The Astrophysical Journal, 810:72 (18pp), 2015 September 1 doi:10.1088/0004-637X/810/1/72

PREDICTIONS FOR ULTRA-DEEP RADIO COUNTS OF STAR-FORMING GALAXIES

Claudia Mancuso[1], Andrea Lapi[1,2], Zhen-Yi Cai[3], Mattia Negrello[4], Gianfranco De Zotti[1,4], Alessandro Bressan[1], Matteo Bonato[4], Francesca Perrotta[1], and Luigi Danese[1]
[1] Astrophysics Sector, SISSA, Via Bonomea 265, I-34136 Trieste, Italy; cmancuso@sissa.it
[2] Dipartimento di Fisica, Università "Tor Vergata," Via della Ricerca Scientifica 1, I-00133 Roma, Italy
[3] CAS Key Laboratory for Research in Galaxies and Cosmology, Department of Astronomy, University of Science and Technology of China, Hefei, Anhui 230026, China
[4] INAF—Osservatorio Astronomico di Padova, Vicolo dell'Osservatorio 5, I-35122 Padova, Italy
Received 2015 February 20; accepted 2015 July 29; published 2015 September 1

ABSTRACT

We have worked outty predictions for the radio counts of star-forming galaxies down to nJy levels, along with redshift distributions down to the detection limits of the phase 1 Square Kilometer Array MID telescope (SKA1-MID) and of its precursors. Such predictions were obtained by coupling epoch-dependent star formation rate (SFR) functions with relations between SFR and radio (synchrotron and free–free) emission. The SFR functions were derived taking into account both the dust-obscured and the unobscured star formation, by combining far-infrared, ultraviolet, and Hα luminosity functions up to high redshifts. We have also revisited the South Pole Telescope counts of dusty galaxies at 95 GHz, performing a detailed analysis of the Spectral Energy Distributions. Our results show that the deepest SKA1-MID surveys will detect high-z galaxies with SFRs two orders of magnitude lower compared to *Herschel* surveys. The highest redshift tails of the distributions at the detection limits of planned SKA1-MID surveys comprise a substantial fraction of strongly lensed galaxies. We predict that a survey down to 0.25 μJy at 1.4 GHz will detect about 1200 strongly lensed galaxies per square degree, at redshifts of up to 10. For about 30% of them the SKA1-MID will detect at least 2 images. The SKA1-MID will thus provide a comprehensive view of the star formation history throughout the re-ionization epoch, unaffected by dust extinction. We have also provided specific predictions for the EMU/ASKAP and MIGHTEE/MeerKAT surveys.

Key words: galaxies: evolution – galaxies: starburst – infrared: galaxies – radiation mechanisms: general – radio continuum: galaxies

1. INTRODUCTION

There are several well established diagnostic tools for measuring the star formation rates (SFRs) in galaxies, each with its own strengths and weaknesses (see Kennicutt & Evans 2012, for a comprehensive review). The ultraviolet (UV) and the Hα luminosities are among the best direct tracers of the emission from young stars, so that the SFR is simply proportional to the luminosity. These diagnostics, however, are highly sensitive to dust extinction and may miss obscured star formation. The latter is measured by the far-infrared (far-IR)/sub-mm luminosity due to dust reprocessing of the emission from newly formed stars. But the dust heating is not always dominated by young stars: older stellar populations can contribute as well. Both the UV/Hα and the FIR diagnostics may also be contaminated by emissions from active galactic nuclei (AGNs).

Ever since radio surveys reached sub-mJy flux density levels (Windhorst et al. 1985), they have proven to be a primary means of identifying star-forming galaxies at high redshift (e.g., Bonzini et al. 2013). Observations have solidly demonstrated a tight correlation between the low-frequency radio continuum, due to synchrotron emission of relativistic electrons mostly produced by supernovae, and the far-IR emission of galaxies, legitimizing its application as an SFR tracer (see Helou et al. 1985; Condon 1992; Yun et al. 2001; Ivison et al. 2010; Jarvis et al. 2010; Bourne et al. 2011; Mao et al. 2011). A word of caution is in order, however, because the physical basis of this relation is not fully understood. In actuality, there are many physical processes, such as the propagation of relativistic electrons, the strength and structure of the magnetic field, and the size and composition of dust grains, that must cooperate to produce this relation (Bell 2003; Lacki et al. 2010). As a consequence it is not a given that this relation also applies to redshift/luminosity ranges where the available data are insufficient to test it precisely. In addition, the synchrotron emission could be contaminated, even by a large factor, by faint nuclear radio activity, and this would bias the estimation of the SFR.

A more direct radio SFR tracer is the free–free emission from the gas ionized by massive young stars (Murphy 2009; Murphy et al. 2015). Because it is directly proportional to the production rate of ionizing photons it provides a measure of the SFR without the complication of dust attenuation that is encountered in the optical/UV. It has a flat spectrum and is expected to show up at frequencies of tens of GHz. The interpretation of data at these frequencies may be complicated by the presence of "anomalous" dust emission (Planck Collaboration XX et al. 2011 and the references therein) attributed to spinning dust grains (e.g., Draine & Lazarian 1998). However, a significant contribution of this component to the global emission of galaxies has yet been proven (Murphy et al. 2012; Planck Collaboration XXV et al. 2014).

The current deepest radio surveys (see de Zotti et al. 2010 for a review) have not been carried out at frequencies high enough or are not deep enough to see the transition from the synchrotron to the free–free dominance. Only with the advent of the Square Kilometer Array (SKA), and partially with its

precursors, can we expect to efficiently select high-z star-forming galaxies via their free–free emission.

In this paper we carry out a thorough investigation of the radio counts and redshift distributions of star-forming galaxies, down to the flux density levels that can be reached by the SKA. Our predictions rely on a state-of-the-art model (Cai et al. 2014) that accounts for the evolution of the cosmic SFR function up to $z \simeq 10$, as measured by a combination of FIR, UV, and Hα data. An outline of the model is presented in Section 2. The redshift-dependent SFR function is translated into the evolving radio luminosity function, taking into account both synchrotron and free–free emissions, using the calibrations by Murphy et al. (2011). In Section 3 we tune the correlation between the SFR and the synchrotron luminosity in order to match the observational determination of the local luminosity function of star-forming galaxies (Mauch & Sadler 2007). This allows us to reproduce the available multi-frequency source counts. Those of star-forming galaxies at 95 GHz provided by the South Pole Telescope (SPT) survey (Mocanu et al. 2013), that are the most sensitive to the free–free emission, have been reassessed performing a more accurate discrimination between star-forming galaxies and radio-loud AGNs. With the radio luminosity function at each redshift it is straightforward to work out predictions for counts and redshift distributions of star-forming galaxies. In Section 4 we show a selection of the results for the frequency range 1.4–30 GHz and compare the coverage of the SFR–z plane by *Herschel*, optical/UV surveys, and the phase 1 SKA-MID. Section 5 explores possible synergies with deep optical/near-infrared (near-IR) surveys. Finally, Section 6 summarizes our main conclusions.

Throughout this paper we adopt a flat ΛCDM cosmology, with matter density $\Omega_{\rm m} = 0.32$, $\Omega_{\rm b} = 0.049$, $\Omega_\Lambda = 0.68$, Hubble constant $h = H_0/100$ km s^{-1} Mpc$^{-1} = 0.67$, spectrum of primordial perturbations with index $n = 0.96$, and normalization $\sigma_8 = 0.83$ (Planck Collaboration XVI et al. 2014).

2. OUTLINE OF THE MODEL

As illustrated by the right panel of Figure 8 of Madau & Dickinson (2014) and by Figure 10 of Cai et al. (2014), the *mean* dust attenuation is low at $z \gtrsim 6$, when the metallicity of the intergalactic medium is lower than the solar value, $Z_\odot$, by a factor $\lesssim 10^{-3}$ (Figure 14 of Madau & Dickinson 2014). Thus, at these redshifts measurements at UV wavelengths are likely to be a reliable SFR diagnostic for most galaxies, although a few galaxies with high SFRs and substantial dust extinction have been found (Riechers et al. 2013; Watson et al. 2015). Great progress has been made in recent years in the determination of UV luminosity functions at high z, up to $z \sim 10$ (Bouwens et al. 2008, 2011a, 2011b, 2015; Oesch et al. 2012, 2013, 2014; Smit et al. 2012; McLure et al. 2013; Schenker et al. 2013), with the aim of reconstructing the history of the cosmic re-ionization.

The mean dust attenuation increases rapidly with decreasing z, down to $z \sim 1$–1.5, where it peaks, to decline at still lower z. In the range $1 \lesssim z \lesssim 3$, including the peak in the cosmic SFR density, the star formation is heavily dust-enshrouded, so that the IR (8–1000 μm) luminosity is an accurate SFR measure. At the other redshifts the safest approach combines UV with IR measurements. In dealing with the latter, we need to be aware that, especially at low redshifts, a significant contribution to dust heating may be due to older stellar populations.

A detailed study of the evolution of the SFR function across the cosmic history was carried out by Cai et al. (2013), focusing on IR data, and by Cai et al. (2014) at $z \gtrsim 2$, focusing on UV and Lyα data but also taking into account dust attenuation and re-emission. These studies build on the work by Granato et al. (2004), further developed by Lapi et al. (2006, 2011, 2014) and Mao et al. (2007). The underlying scenario relies on the results of intensive N-body simulations and semi-analytic studies (e.g., Zhao et al. 2003; Lapi & Cavaliere 2011; Wang et al. 2011) that show that pre-galactic halos undergo an early phase of fast collapse, including a few major merger events, during which the central regions rapidly reach a dynamical quasi-equilibrium. A slow growth of the halo outskirts in the form of many minor mergers and diffuse accretion follows. This second stage has little effect on the inner potential well where the visible galaxy resides.

The baryons falling into the potential wells created during the fast collapse phase are shock-heated to the virial temperature. The gas cools down giving rise to star formation. At the same time it loses angular momentum, e.g., by the effect of the radiation drag, and flows toward the central regions, accreting onto the central supermassive black hole. These processes are governed by a set of equations, reported in the appendix of Cai et al. (2013), that take into account the energy feedback from supernovae and from the active nucleus. The model includes a self consistent treatment of the chemical evolution of the ISM, calculated using the standard equations and stellar nucleosynthesis prescriptions, as written down, for instance, in Romano et al. (2002). The chemical evolution controls the evolution of the dust abundance, hence the dust absorption and re-emission.

In this framework Cai et al. (2014) worked out a model for the evolution of the UV and Lyα luminosity functions of high-redshift ($z \gtrsim 2$) galaxies, taking into account their chemical evolution and the associated evolution of dust extinction. The model yields good fits of the observed luminosity functions at all redshifts at which they have been measured and provides a physical explanation for the weak observed evolution of both luminosity functions between $z = 2$ and $z = 6$.

While at high z the high star formation efficiency implied by the scenario briefly sketched above applies to most galaxies, at lower z a dichotomy arises (see, e.g., Bernardi et al. 2010). Early-type galaxies and massive bulges of Sa galaxies are composed of relatively old stellar populations with mass-weighted ages $\gtrsim$8–9 Gyr. They must therefore have been forming most of their stars over short timescales at $z \gtrsim 1-1.5$ and must have dominated the cosmic SFR at high z. Instead, the disc components of spirals and the irregular galaxies are characterized by significantly younger stellar populations and star formation activity continuing up to the present time. They are therefore the dominant star formers at $z \lesssim 1.5$.

Cai et al. (2013) modeled the cosmological evolution of the SFR function of proto-spheroidal galaxies (the progenitors of present day early-type galaxies and of massive bulges of disc galaxies) during their dust-enshrouded star formation phase, and the concomitant evolution of their active nuclei. This model provides a physical explanation for the observed positive evolution of both galaxies and AGNs up to $z \approx 2.5$, and for the negative evolution at higher redshifts, for the sharp transition from Euclidean to extremely steep counts at (sub-)mm wavelengths, as well as for the (sub-)mm counts of strongly lensed galaxies, which are hard to account for by alternative,

physical, or phenomenological approaches. Furthermore, as shown by Xia et al. (2012) and Cai et al. (2013), the halo masses inferred both from the angular correlation function of detected sub-mm galaxies (Cooray et al. 2010; Maddox et al. 2010) and from the power spectrum of fluctuations of the cosmic infrared background (Amblard et al. 2011; Planck Collaboration XVIII et al. 2011; Viero et al. 2013; Planck Collaboration XXX et al. 2014) are fully consistent with those implied by this scenario, while they are larger than those implied by the major mergers plus the top-heavy initial stellar mass function (Baugh et al. 2005; Lacey et al. 2010) and smaller than those implied by cold flow models (Davé et al. 2010).

Late-type galaxies follow a different evolutionary track. The evolution of the IR luminosity function of these objects was described by Cai et al. (2013) using a phenomenological approach, considering two populations with different spectral energy distributions (SEDs) and different evolutionary properties: "normal" late-type galaxies, with low evolution and low dust temperatures and rapidly evolving starburst galaxies, with warmer dust temperatures.

The evolution of late-type "normal" and "starburst" galaxies is described using a phenomenological parametric approach. For the starburst population, power-law density and luminosity evolution [$\Phi^\star(z) = \Phi^\star(z=0) \times (1+z)^{\alpha_\Phi}$; $L^\star(z) = L^\star(z=0) \times (1+z)^{\alpha_L}$] up to $z_{\rm break} = 1$ was assumed. The normal galaxy population has only a mild luminosity evolution up to the same value of $z_{\rm break}$, as indicated by chemo/spectrophotometric evolution models. At $z > z_{\rm break}$ both $\Phi^\star(z)$ and $L^\star(z)$ are kept to the values at $z_{\rm break}$ multiplied by a smooth cut-off function. For further details and the values of the parameters, see Cai et al. (2013).

The model fits a broad variety of data[5]: multi-frequency and multi-epoch luminosity functions of galaxies and AGNs, redshift distributions, and number counts (total and per redshift bins). It also accurately accounts for the recent counts and redshift distribution of strongly lensed galaxies detected by the South Pole Telescope (SPT; Mocanu et al. 2013; Weiß et al. 2013) as shown by Bonato et al. (2014).

When the dust heating is dominated by young stars and the effective optical/UV optical depth is high, the total (8–1000 μm) IR luminosity, $L_{\rm IR}$, is a good measure of the SFR. More generally, the IR luminosity is the sum of a "warm" dust component heated by young stars and of a "cold" dust (or "cirrus") component, heated by the general radiation field probably dominated by older stars. Obviously the only tracer of the SFR is the first component. This issue was investigated by Clemens et al. (2013) using a complete sample of local star-forming galaxies detected by the *Planck* satellite. We adopt the relation between SFR and $L_{\rm IR}$ derived by these authors:

$$\log\left({\rm SFR}/M_\odot\ {\rm yr}^{-1}\right) = -9.6 + \log\left(L_{\rm IR}/L_\odot\right) - \left(\frac{2.0}{\log\left(L_{\rm IR}/L_\odot\right) - 7.0}\right), \quad (1)$$

As expected, high IR luminosities generally correspond to high SFRs, i.e., to a dominant "warm" dust component. Note that calibrations of SFR diagnostics generally depend on the adopted initial mass function (IMF). In the above equation we have adopted the one by Chabrier (2003). According to Figure 1 of Chomiuk & Povich (2011) the differences with the calibrations using the Kroupa (2001) IMF (Murphy et al. 2011, 2012; Kennicutt & Evans 2012) are $\lesssim$10% and will be neglected. The Cai et al. (2013) model deals only with dust-obscured star formation. To get a comprehensive view of the evolution of the SFR function of late-type galaxies, including the unobscured star formation, we have enhanced it it by taking into account optical/UV SFR indicators, again adopting a parametric approach for evolution.[6] Details are given in the Appendix A.

The SFR functions at several redshifts, obtained combining IR, UV, and Hα survey data, are shown in Figure 1, where also the SFR functions derived from the UV luminosity functions using the Kennicutt & Evans (2012) calibration but without the extinction correction are plotted (thin solid lines). Below an SFR $\simeq$ 0.1–1 $M_\odot$ yr^{-1}, depending on z, the SFR functions derived from the IR luminosity functions fall below those derived from the UV and Hα luminosity functions without extinction corrections, implying that extinction becomes negligible for low SFRs. The opposite happens for higher SFRs. The model tends to underpredict the brightest points of the luminosity functions. We note, however, that the discrepancy is of the order of differences among estimates from different surveys. This suggests that the data points are affected by cosmic variance due to the relatively small area studied; the rare objects with the highest luminosities are preferentially detected in areas where they are overdense.

While at $z < 1.5$ the observationally determined SFR functions are fully accounted for by UV measurements with the appropriate extinction corrections, at higher redshifts UV surveys miss most of the galaxies with the highest SFRs, which are heavily dust-obscured and therefore show up at far-IR/sub-mm wavelengths. According to our model, the dominant contribution at the highest SFRs at $z \gtrsim 1.5$ comes from proto-spheroidal galaxies.

Figure 2 presents a synoptic view of the cosmological evolution of the cosmic SFR function up to $z = 8$, as given by the model described above, including the contributions of normal late-type, starburst, and proto-spheroidal galaxies. This function has a complex evolutionary behavior. Its knee value increases with z up to $z \simeq 2-3$ and declines at higher redshifts; its slopes above and below the knee also change with redshift. Aversa et al. (2015) have worked out approximate analytic expressions providing a sensible rendition of the observational determinations of the redshift-dependent SFR function. To this end they used a modified Schechter function with evolving characteristic luminosity and slopes. The luminosity function [Mpc^{-3} log(SFR)$^{-1}$] writes

$$\phi_{\rm SFR}(z) = \Phi(z)\left[\frac{\rm SFR}{{\rm SFR}_\star(z)}\right]^{1-\alpha(z)} \times \exp\left\{-\left[\frac{\rm SFR}{{\rm SFR}_\star(z)}\right]^{\omega(z)}\right\}, \quad (2)$$

[5] See http://people.sissa.it/~zcai/galaxy_agn/ or http://staff.ustc.edu.cn/~zcai/galaxy_agn/index.html

[6] Early-type galaxies are in passive evolution at low z and their early unobscured star formation phases are dealt with by Cai et al. (2014).

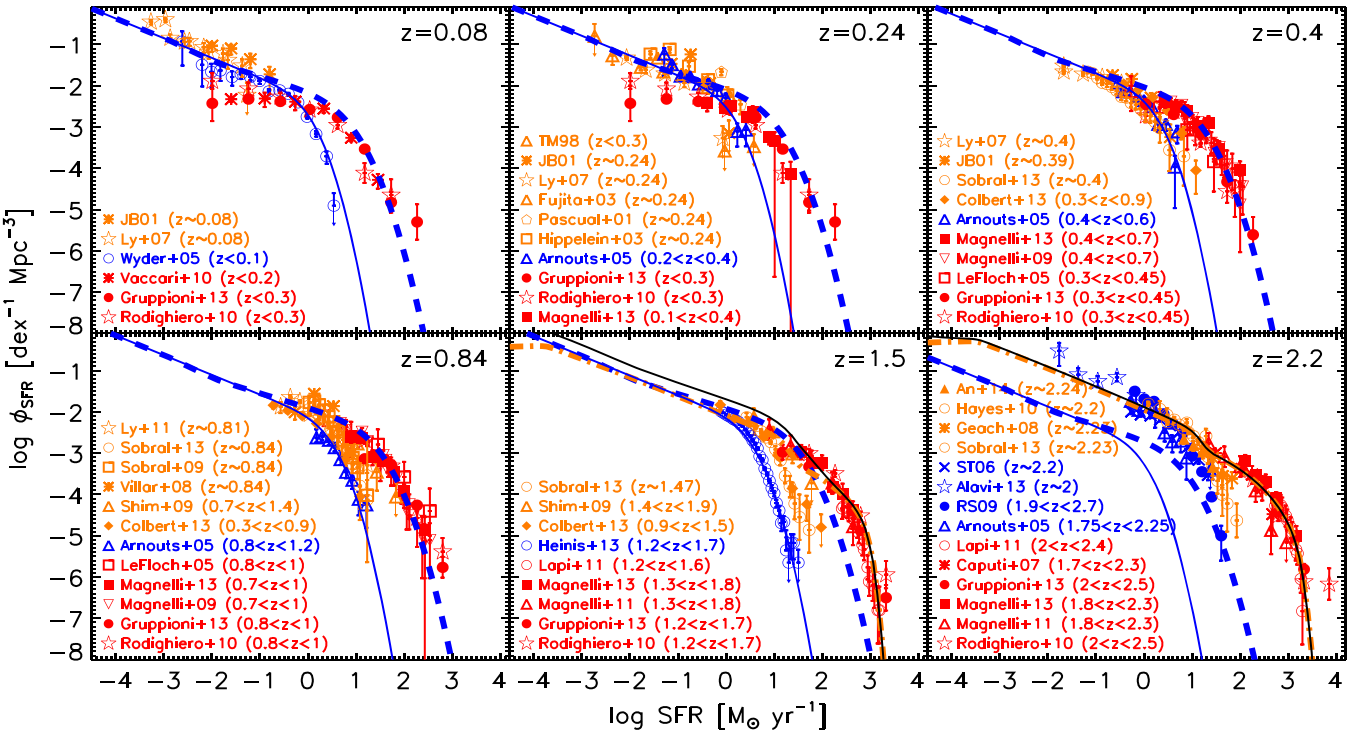

Figure 1. SFR functions at several redshifts. The blue lines show the SFR functions derived from the UV luminosity functions given by the phenomenological model for late-type galaxies with and without the extinction correction (dashed and thin solid lines, respectively). The dot–dashed orange lines show the contributions given by the physical model for proto-spheroids with a minimum halo mass $M_{\rm vir}^{\rm min} = 10^{8.5}\,M_\odot$. The thick black lines show the sum of the contributions from late-type galaxies, after the extinction correction, and of proto-spheroids. The red data points are estimates from far-IR measurements (Caputi et al. 2007; Rodighiero et al. 2010; Lapi et al. 2011; Magnelli et al. 2011, 2013; Gruppioni et al. 2013). The blue data points are from UV measurements (Steidel et al. 1999; Arnouts et al. 2005; Wyder et al. 2005; Sawicki & Thompson 2006; Reddy & Steidel 2009; Heinis et al. 2013; Alavi et al. 2014). The orange data points are from Hα measurements (Tresse & Maddox 1998; Jones & Bland-Hawthorn 2001; Pascual et al. 2001; Fujita et al. 2003; Hippelein et al. 2003; Ly et al. 2007, 2012; Geach et al. 2008; Villar et al. 2008; Sobral et al. 2009, 2013; Hayes et al. 2010). The conversions of attenuated UV and Hα luminosities to SFRs are done using the Kennicutt & Evans (2012) calibrations, i.e., $\log({\rm SFR}/[M_\odot\,{\rm yr}^{-1}]) = \log(L_{\rm FUV}/[L_\odot]) - 9.825$ and $\log({\rm SFR}/[M_\odot\,{\rm yr}^{-1}]) = \log(L_{\rm H\alpha}/[{\rm erg\,s}^{-1}]) - 41.270$, respectively. The conversion of the IR luminosity to SFR was done using Equation (1), which takes into account that a substantial contribution to dust heating in galaxies with low SFRs comes from old stellar populations. Comparing the SFRs estimated from the UV or from the Hα luminosities with those inferred from the IR luminosities it is apparent that the former are is increasingly underestimated with increasing SFR and redshift, consistent with the findings by Reddy et al. (2012) and Burgarella et al. (2013).

where

$$\begin{aligned}
\log\Phi(z)\left[{\rm Mpc}^{-3}\log({\rm SFR})^{-1}\right] &= -2.4 - 2.3\,\chi \\
&\quad + 6.2\,\chi^2 - 4.9\,\chi^3, \\
{\rm logSFR}_\star(z)\left[M_\odot\ {\rm yr}^{-1}\right] &= 1.1 + 3.2\,\chi \\
&\quad - 1.4\,\chi^2 - 2.1\,\chi^3, \\
\alpha(z) &= 1.2 + 0.5\,\chi \\
&\quad - 0.5\,\chi^2 + 0.2\,\chi^3, \\
\omega(z) &= 0.7 - 0.15\,\chi \\
&\quad + 0.16\,\chi^2 + 0.01\,\chi^3,
\end{aligned}$$

with $\chi = \log(1+z)$. Note that the above equation is simply meant to provide an analytic rendition of the complex evolution of the SFR function, for use in practical applications. As pointed out by Aversa et al. (2015) the non-homogeneous nature of the data sets used to derive the SFR functions and the diverse systematics affecting them does not warrant the use of formal fitting procedures.

3. RELATIONS BETWEEN RADIO EMISSION AND SFR

3.1. Calibration of the Relation between SFR and Synchrotron Emission

A calibration of the SFR-synchrotron luminosity relation was obtained by Murphy et al. (2011) using Starburst99 (Leitherer et al. 1999) with a Kroupa (2001) IMF and specific choices for the metallicity and the star formation history. We have slightly modified their relation, including a steepening of the synchrotron spectrum by $\Delta\alpha = 0.5$ above a break frequency of 20 GHz to take into account electron ageing effects (Banday & Wolfendale 1991). The SFR-synchrotron luminosity relation then can be written as

$$\bar{L}_{\rm sync} \simeq 1.9\times10^{28}\left(\frac{\rm SFR}{M_\odot{\rm yr}^{-1}}\right)\left(\frac{\nu}{\rm GHz}\right)^{-0.85} \times\left[1+\left(\frac{\nu}{20\ {\rm GHz}}\right)^{0.5}\right]^{-1}{\rm erg\,s^{-1}\,Hz^{-1}}. \quad (3)$$

The high-frequency synchrotron emission can be further suppressed at high z because of the energy losses of relativistic

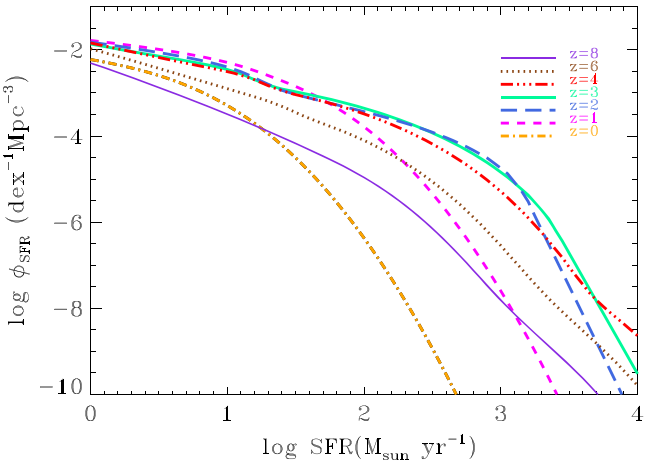

Figure 2. Synoptic view of the evolution of the cosmic SFR function as given by the model described in Section 2. The luminosity function at each redshift includes the contributions of normal late-type, starburst, and proto-spheroidal galaxies.

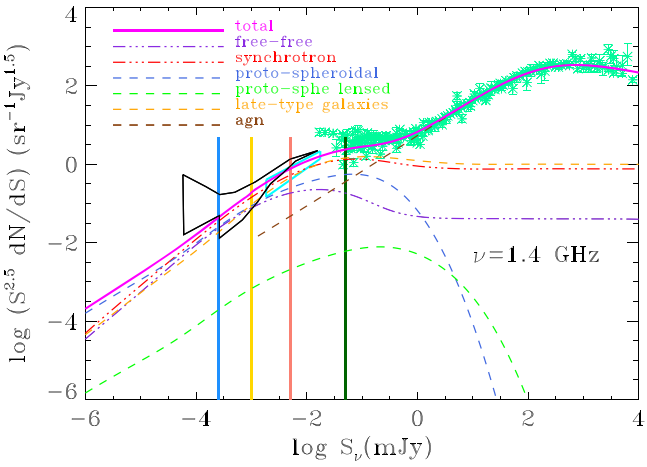

Figure 3. Euclidean normalized differential counts at 1.4 GHz compared with model predictions. Above ∼1 mJy the counts are dominated by canonical radio-loud active galactic nuclei (AGNs) while star-forming galaxies take over at fainter flux densities. The dashed brown line shows the model for radio AGNs by Massardi et al. (2010). The other dashed lines show the contributions of the star-forming populations considered in this paper (unlensed and strongly lensed proto-spheroids and late-type galaxies). The two triple-dot-dashed lines show the total synchrotron and free–free emissions from these populations. References for the data points can be found in de Zotti et al. (2010). The cyan and the black polygons show the ranges of 1.4 GHz counts consistent with the $P(D)$ distributions by Condon et al. (2012) and Vernstrom et al. (2014), respectively. Note that these $P(D)$ analyses rule out the sub-mJy counts as high as the Owen & Morrison (2008) estimates. As argued by Condon et al. (2012) the high counts may result from the large and difficult corrections for the effects of partial resolution; the quoted $P(D)$ data do not need significant resolution corrections. The vertical lines correspond, from left to right, to the 5σ detection limits of the planned SKA1-MID surveys to unresolved sources: 0.25 μJy (blue), 1 μJy (yellow), 5 μJy (pink). Given the resolution of these surveys (≃0.″5; Prandoni & Seymour 2014) it is likely that a fraction of sources (especially bright, nearby galaxies) will be resolved out so that the surveys will not be 100% complete at the quoted limits. However, the array configuration proposed, which delivers an essentially flat point source sensitivity over a large range of synthesized beams, will overcome this problem. The 5 μJy limit applies also to the Tier 2 MIGHTEE survey (MeerKAT), while the dark green line shows the EMU (ASKAP) survey 5σ limit. Again, the limits refer to unresolved sources. The MIGHTEE and EMU surveys have a lower resolution than the SKA1-MID ones: 8.″3–3.″5 in the case of Tier 2 MIGHTEE (http://www.ast.uct.ac.za/arniston2011/vdheyden.pdf) and 10″ in the case of EMU (Norris et al. 2011).

electrons due to inverse Compton scattering off the cosmic microwave background (CMB) photons, whose energy density increases as $(1+z)^4$ (Carilli et al. 2008; Murphy 2009; Norris et al. 2013). Also it should be noted that, at variance with free–free and UV emissions, which are a measure of the current SFR, the synchrotron emission is delayed by $\sim 10^7$ years, the main sequence lifetime of massive stars whose supernova explosions are responsible for the production of the relativistic electrons (Clemens et al. 2008). At high z the fraction of galaxies younger than $\sim 10^7$ years, which lack relativistic electrons, and hence the synchrotron emission, increases.

Since these effects are not taken into account in our calculations because we lack an adequate model for them, we may overestimate the faint counts and the high-z tails of the redshift distributions. However, the overestimate of the total radio luminosity is unlikely to be large because even at 1.4 GHz (and more so at higher frequencies), at flux densities below the current observational limits the free–free contribution is comparable to the synchrotron one (see Figure 3).

In translating the SFR function into a synchrotron luminosity function we need to take into account that the correlation between the SFR and the radio luminosity has a substantial dispersion. Furthermore, it has long been suggested that the synchrotron radiation from low-SFR galaxies is somewhat suppressed (Klein et al. 1984; Chi & Wolfendale 1990; Price & Duric 1992), although this view is controversial (Condon 1992). A comparison of the local SFR function with the local radio luminosity function at 1.4 GHz (dominated by synchrotron emission; Mauch & Sadler 2007) shows that the latter is flatter than the former at low luminosities. If the corresponding portion of the SFR function was inferred from far-IR data one could argue that it is overestimated since a fraction of the far-IR emission could be due to dust heated by evolved stars. But in fact it was derived from Hα measurements and therefore it is not susceptible to such a problem. To reconcile the SFR function with the radio luminosity function we need to assume a nonlinear $L_{\rm sync}$–SFR relation. Following Massardi et al. (2010) we adopt a relation of the form:

$$L_{\rm sync}(\nu) = \frac{L_{\star,{\rm sync}}(\nu)}{\left(L_{\star,{\rm sync}}/\bar{L}_{\rm sync}\right)^{\beta} + \left(L_{\star,{\rm sync}}/\bar{L}_{\rm sync}\right)}, \qquad (4)$$

where $\bar{L}_{\rm sync}$ is given by Equation (3) and $\beta = 3$. This equation converges to Equation (3) for $\bar{L}_{\rm sync} \gg L_{\star,{\rm sync}} = 0.886\bar{L}_{\rm sync}$ (SFR $= 1\ M_\odot\ {\rm yr}^{-1}$). At 1.4 GHz, $L_{\star,{\rm sync}} \simeq 10^{28}$ erg s^{-1} Hz^{-1}. Applying this relation to the redshift-dependent SFR functions presented in Section 2 (see Figure 1) and further adopting for the $L_{\rm radio}$–SFR relation a dispersion of $\sigma_{\rm radio} = 0.4$ dex we get agreement with the Mauch & Sadler (2007) luminosity function (see Figure 4) as well as with the sub-mJy counts at 1.4 GHz, dominated by emission from star-forming galaxies. The model counts, obtained by adding those of radio-loud AGNs yielded by the Massardi et al. (2010) model,[7] are shown in Figure 3.

[7] Tabulations of the radio-loud AGN counts yielded by the model at several frequencies are publicly available at http://w1.ira.inaf.it/rstools/srccnt/srccnt_tables.html

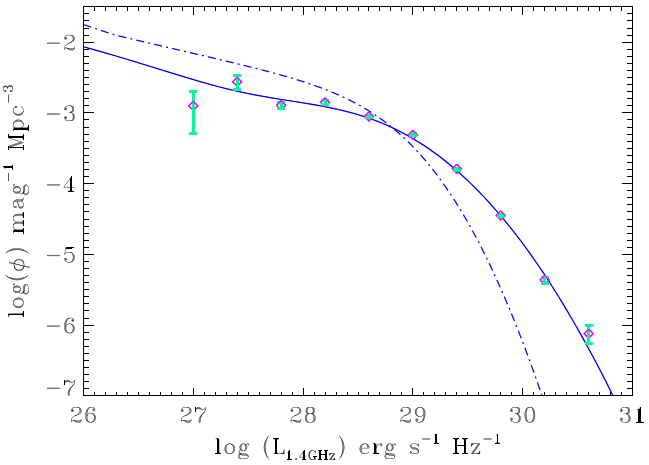

Figure 4. Synchrotron luminosity function of local star-forming galaxies derived from the local SFR function using the nonlinear $L_{\rm radio}$–SFR relation (see Equation (4)) and a dispersion of $\sigma_{\rm radio} = 0.4$ dex around the mean relation, compared with the observational determination by Mauch & Sadler (2007). The luminosity function obtained assuming a simple proportionality between $L_{\rm radio}$ and the SFR (Equation (3)) is also shown for comparison (dot–dashed line). The dispersion $\sigma_{\rm radio}$ raises the bright portion of the luminosity function while Equation (4) flattens the faint part.

3.2. Calibration of the Relation between SFR and Free–Free Emission

We have rewritten the relation between SFR and free–free emission derived by Murphy et al. (2012) as

$$L_{\rm ff} = 3.75 \times 10^{26} \left(\frac{\rm SFR}{M_\odot\ {\rm yr}^{-1}}\right)\left(\frac{T}{10^4\ {\rm K}}\right)^{0.3} \times {\rm g}(\nu, T) \exp\left(-\frac{h\nu}{kT}\right), \quad (5)$$

where T is the temperature of the emitting plasma and ${\rm g}(\nu, T)$ is the Gaunt factor for which we adopt the approximation of Draine & Bruce (2011), which improves over earlier approximations

$${\rm g}(\nu, T) = \ln\left\{\exp\left[5.960 - \frac{\sqrt{3}}{\pi}\ln\left(Z_i\frac{\nu}{\rm GHz}\left(\frac{T}{10^4{\rm K}}\right)^{-1.5}\right)\right] + \exp(1)\right\}, \quad (6)$$

where Z_i is the charge of ions and T is their temperatures. This equation reproduces the Murphy et al. (2012) calibration at the calibration frequency (33 GHz) for a pure hydrogen plasma ($Z_i = 1$) and $T = 10^4$ K. At the other frequencies that are relevant here the differences due to the different approximations for the Gaunt factor are small. We will adopt the above values of Z_i and T throughout the paper.

We have used Equation (5) to convert the redshift-dependent SFR functions to free–free luminosity functions. To compute the counts of star-forming galaxies at 95 GHz, where an observational estimate has been obtained thanks to the SPT survey (Mocanu et al. 2013), we need to take into account that the measured flux densities include, in addition to the free–free emission, contributions from thermal dust and from the synchrotron emission (see Figure 5). All of these contributions were taken into account using the $L_{\rm ff}$–SFR and $L_{\rm sync}$–SFR relations given above, plus the $L_{\rm IR}$–SFR relation appropriate for each galaxy population: Equation (1) for late-type galaxies and

$$L_{\rm IR} = 3.1 \times 10^{43}\left(\frac{\rm SFR}{M_\odot\ {\rm yr}^{-1}}\right) {\rm erg\ s}^{-1}, \quad (7)$$

for proto-spheroidal galaxies (Cai et al. 2013). This calibration is essentially identical to the empirical relation derived by Murphy et al. (2012). To get down to any chosen frequency we used the SEDs for the three populations of star-forming galaxies ("cold" and "warm" late-type galaxies, and high-z proto-spheroidal galaxies) considered by Cai et al. (2013), adding the free–free and synchrotron emissions given by Equations (3) and (5).

The model counts turned out to be substantially below those estimated by Mocanu et al. (2013). The statistical approach adopted by these authors, however, did not appear completely reliable. They used the α_{220}^{150} spectral indices to classify their sources, taking $\alpha_{220}^{150} = 1.5$ as the boundary between dust-dominated galaxies ($\alpha_{220}^{150} > 1.5$) and radio-loud AGNs (synchrotron-dominated, in their terminology). They computed the probability that their posterior value for α_{220}^{150} was greater than the boundary value and interpreted it as the probability for a source to be dust-dominated. The 95 GHz differential counts were calculated as the sum of the probabilities $P(\alpha_{220}^{150} > 1.5)$ that the sources in a given flux density ($S_{\rm 95GHz}$) range are dusty. Since at 95 GHz the dusty galaxies are a small fraction of detected sources, this approach may easily overestimate the counts because due to the large uncertainties on α_{220}^{150}, many radio-loud AGNs have a non-zero probability of being dust-dominated. The sum of these low probabilities may give a count comparable to or even larger than the count of the rare truly dusty galaxies.

This argument has motivated us to re-estimate the 95 GHz counts of dusty galaxies using a safer, although lengthier approach. There are 406 95 GHz sources brighter than 12.6 mJy, the 95% completeness limit of the survey. We have checked the SEDs of all of them, collecting the photometric data available in the NASA/IPAC Extragalactic Database (NED) plus the *Wide-field Infrared Survey Explorer* (*WISE*; Wright et al. 2010) AllWISE[8] catalog, the Planck Catalog of Compact Sources (Planck Collaboration XXVIII et al. 2014) and the IRAS catalog. We found that only four sources, all with $P(\alpha_{220}^{150} > 1.5) = 1$, are indeed dusty galaxies. They are listed in Table 1 and their SEDs are shown in Figure 5. A fifth source, with $P(\alpha_{220}^{150} > 1.5) \simeq 1$, SJ043643-6204.4, is only 0.368 arcmin away from the very bright red giant Mira variable star R Doradus. Its SPT photometry may be strongly contaminated by emission from dust shrouds that often form around these kinds of stars. For this reason we have discarded this source.

For comparison, the Mocanu et al. (2013) approach yields $\simeq$12 dusty galaxies with $S_{\rm 95GHz} \geqslant 12.6$ mJy. A substantial contribution to the difference with our result comes from sources with $P(\alpha_{220}^{150} > 1.5) \ll 1$. The reassessed integral counts are shown in Figure 6. It is worth mentioning that three out of the four confirmed dusty galaxies have low-frequency radio luminosity in excess of that expected from the mean relation between IR and 1.4 GHz luminosities. The

[8] http://wise2.ipac.caltech.edu/docs/release/allwise/

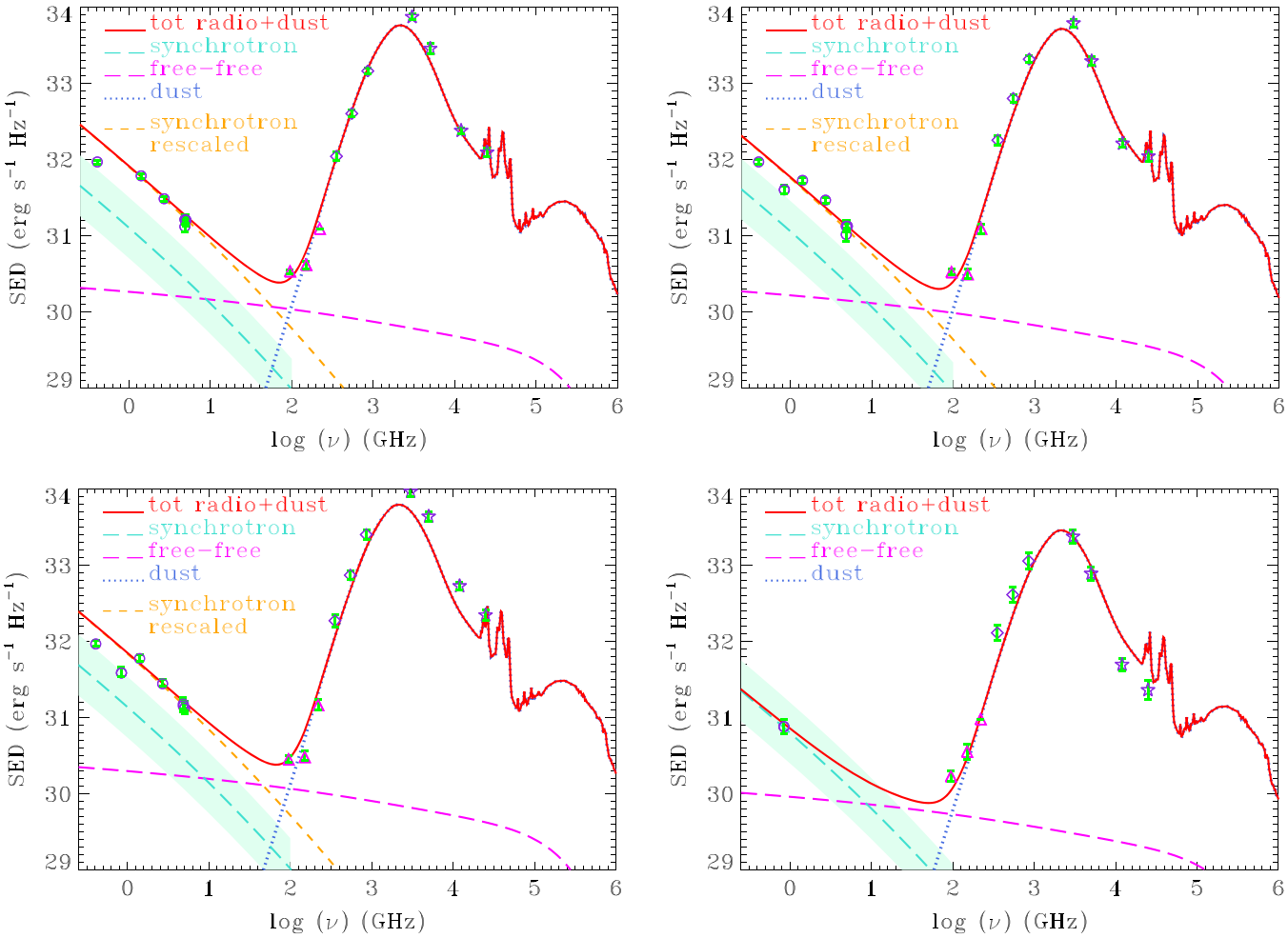

Figure 5. SEDs of 95 GHz selected dusty galaxies in the SPT sample by Mocanu et al. (2013): SPT-SJ041736-6246-8 (top left), SPT-SJ041959-5456-2 (top right), SPT-SJ044540-5914-7 (bottom left), SPT-SJ213629-5433-4 (bottom right). The red curve is a fit made by eye summing the Cai et al. (2013) SED of a cold late-type galaxy (dotted blue line), chosen because the four galaxies are all normal disc galaxies, with the free–free emission given by Equation (5) for the same SFR (long-dashed magenta line) and with the synchrotron emission matching the low-frequency data. For three of the galaxies, such synchrotron emission (short-dashed orange line) is higher than that given by Equation (3), represented by the long-dashed green line. The difference is about twice the dispersion of the relation between the synchrotron luminosity and the SFR (shaded green band; see Section 3.1), yet within the range of values for star-forming galaxies according to Yun et al. (2001). It may thus be not statistically significant, especially taking into account a possible selection effect: the higher synchrotron luminosity helps bring the sources above the detection limit at 95 GHz. However, we cannot rule out alternative explanations such as an additional contribution from a weak active nucleus or excess radio emission arising from radio continuum bridges and tidal tails not associated with star formation, similar to what is observed for so-called "taffy" galaxies (Condon et al. 2002; Murphy 2013). Data points: low-frequency radio flux densities from the NED (open circles); SPT flux densities (triangles); *Planck* flux densities (open diamonds); IRAS flux densities (open stars).

Table 1
Dusty Galaxies in the Mocanu et al. (2013) 95 GHz Sample

Galaxy	Redshift	$S_{95\mathrm{GHz}}$ (mJy)
SJ041736-6246.8	0.00435	25.56
SJ041959-5456.2	0.005017	24.87
SJ044540-5914.7	0.00444	21.2
SJ213629-5433.4	0.002825	12.76

difference is about twice the dispersion of the relation between the synchrotron luminosity and the SFR, yet is within the range of values for star-forming galaxies according to Yun et al. (2001). It may thus be not statistically significant, especially taking into account a possible selection effect: the higher synchrotron luminosity helps bring the sources above the detection limit at 95 GHz. The parameter q, defined by

$$q = \log\left[\frac{\mathrm{FIR}/3.75 \times 10^{12}\ \mathrm{Hz}}{S_{1.4\ \mathrm{GHz}}\left(\mathrm{W\ m^{-2}\ Hz^{-1}}\right)}\right], \quad (8)$$

where

$$\mathrm{FIR}\left(\mathrm{W\ m^{-2}}\right) = 1.26 \times 10^{-14}\left[2.58 S_{60\mu\mathrm{m}}(\mathrm{Jy}) + S_{100\mu\mathrm{m}}(\mathrm{Jy})\right], \quad (9)$$

has values ranging from 1.85 to 2.06 for the aforementioned galaxies, somewhat smaller than the mean value of q for star-forming galaxies ($q = 2.34$ with a dispersion $\sigma = 0.26$; Yun et al. 2001), yet larger than the value $q_{\mathrm{lim}} = 1.64$ proposed by Yun et al. (2001) as the boundary between starburst-dominated and AGN-dominated radio emission. In any case, we cannot rule out alternative explanations such as an additional

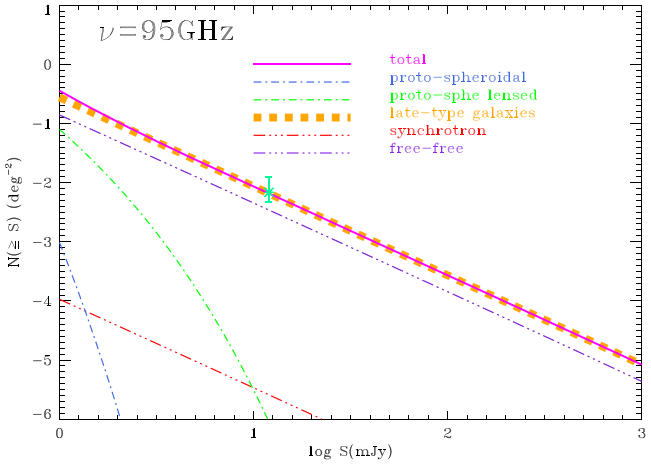

Figure 6. Our reassessment of the integral counts of dusty galaxies at $\nu = 95$ GHz (asterisks with error bars) compared with the expectations from the Cai et al. (2013) model, using for each source populations the complete SEDs that include dust, synchrotron, and free–free emissions. The various lines correspond to the contributions from the different source populations and from the different emission processes, identified in the legend inside the figure.

contribution from a weak active nucleus or excess radio emission arising from radio continuum bridges and tidal tails not associated with star formation, similar to what is observed for so-called "taffy" galaxies (Condon et al. 2002; Murphy 2013).

The SEDs of all the other sources are consistent with the 95 GHz flux density being dominated by synchrotron emission and inconsistent with them being dusty galaxies. As illustrated by Figure 7, this is also the case for the other 4 sources with $P(\alpha_{220}^{150} > 1.5) > 0.6$, including the one with $P(\alpha_{220}^{150} > 1.5) = 0.91$. The radio-source nature of all objects with lower values of $P(\alpha_{220}^{150} > 1.5)$ is even clearer.

Figures 6 and 8 show that we obtain good agreement with the new determination of SPT counts of dusty galaxies at 95 GHz as well as with those by Mocanu et al. (2013) at 150 and 220 GHz. While the 95 GHz counts are dominated by nearby galaxies, those at the higher frequencies include a contribution from high-z strongly lensed proto-spheroidal galaxies; their contribution increases with decreasing flux density (in the ranges covered by the SPT surveys) to the point of becoming dominant at the SPT detection limits.

The model has been further tested at 4.8, 8.4, 15, and 30 GHz (Figure 9). Not surprisingly, the free–free contribution becomes increasingly important at higher and higher frequencies. While at 1.4 GHz the dominant emission is synchrotron, at 8.4 GHz the free–free emission takes over at sub-mJy levels.

4. PREDICTIONS FOR SURVEYS WITH THE SKA AND ITS PRECURSORS

4.1. Number Counts and Redshift Distributions

The plans for SKA Phase 1 (SKA1-MID) will likely include three continuum surveys (in band 2), all at ≃1–1.4 GHz: one over 1000 deg^2 with rms ≃1 μJy/beam, a second one over 30 deg^2 with rms ∼0.2 μJy/beam, and a third over 1 deg^2 with rms ∼50 nJy/beam (Prandoni & Seymour 2014). In addition there will possibly be a deep survey in band 5, at ≃10 GHz, with rms ≃0.3 μJy/beam over 1 deg^2, and an ultra-deep survey again in band 5, at ≃10 GHz with rms ≃0.03 μJy/beam over ≃30 arcmin^2 (see also Murphy et al. 2015).

Deep surveys are also planned with the SKA precursors, like the Australian SKA Pathfinder (ASKAP) and the South African MeerKAT (Norris et al. 2013). The Evolutionary Map of the Universe (EMU) is a project that will use ASKAP to make a deep (5σ limit of 50 μJy beam^{-1}) radio continuum survey of the entire southern sky, extending as far north as $+30°$, i.e., covering about 30,000 deg^2 at ∼1.4 GHz. The MeerKAT International GigaHertz Tiered Extragalactic Exploration (MIGHTEE) Tier 2 will exploit the MeerKAT Phase 2 to observe over 35 deg^2 down to a 5σ limit of 5 μJy beam^{-1}, again at ∼1.4 GHz.

The SKA1-MID, EMU, and MIGHTEE 5σ flux density limits for unresolved sources are indicated by vertical lines in Figure 3. The contributions of the various dusty galaxy populations are shown by the different lines. The "bump" at tens of μJy's is due to late-type galaxies at $z \simeq 1$–1.5. Proto-spheroidal galaxies at higher z become increasingly important at lower flux densities, down to a few hundred nJy's.

The predicted redshift distributions for surveys at the flux density limits mentioned above are shown in Figures 10 and 11. The surface density of galaxies at $z \geqslant 6$ increases rapidly with decreasing flux density. For the 5 σ detection limits of the 1.4 GHz surveys mentioned above it is of ≃10^{-2}, 6.4, 148, and 1013 deg^{-2} for $S_{1.4\,\mathrm{GHz}} > 50$, 5, 1, and 0.25 μJy respectively, implying that the 3 SKA1-MID surveys are expected to detect ≃6400, 4440, and 1013 $z \geqslant 6$ galaxies, respectively, while the MIGHTEE and the EMU surveys should detect about 220 and 300 galaxies at these redshifts, respectively. Figure 10 shows that the SKA1-MID surveys may reach even higher redshifts, allowing us to get a glimpse of the cosmic SFR across the re-ionization epoch, overcoming limitations by dust extinction. We expect the detection of about 120, 163, and 58 galaxies at $z > 8$ by the 3 SKA1-MID surveys down to $S_{1.4\mathrm{GHz}} = 5$, 1, and 0.25 μJy, respectively.

As illustrated by Figure 11, the planned band 5 surveys will also reach very high redshifts (see also Murphy et al. 2015). We predict the detection of ≃16.5 and ≃5.5 $z > 6$ galaxies with the deep and the ultra-deep survey, respectively. These estimates include the contribution of dust emission that is significant for the highest redshift galaxies (see Figure 5). However, dust emission is likely under-abundant in most galaxies at $z > 6$ (Muñoz & Loeb 2011; Cai et al. 2014; Capak et al. 2015) because there is probably not enough time for a substantial dust enrichment of the galaxy interstellar medium. However, galaxies with high SFRs and substantial dust extinction have been reported (Riechers et al. 2013; Watson et al. 2015), and the timescale for dust enrichment is poorly known (Mancini et al. 2015). SKA1-MID data will provide key information in this respect.

In Figure 12 we compare the SKA1-MID potential in measuring the evolution of the cosmic SFR to the results of *Herschel* and of the deepest UV and Hα surveys. The planned SKA1-MID surveys can detect galaxies with SFRs ranging from less than one $M_\odot\,\mathrm{yr}^{-1}$ for $z \lesssim 1$ to less than hundreds of $M_\odot\,\mathrm{yr}^{-1}$ for $z \lesssim 7$. This is an improvement by more than two orders of magnitude compared to *Herschel* results and will allow us to determine the dust-enshrouded star formation history up to much higher redshifts. The deepest rest-frame UV surveys do better, but only for dust-free galaxies. The deepest ALMA maps at 1.1 and 1.3 mm (Carniani et al. 2015) reach lower SFRs than SKA1-MID at $z \gtrsim 3$, thanks to the negative K-correction. We note that ALMA is not designed to be a pure

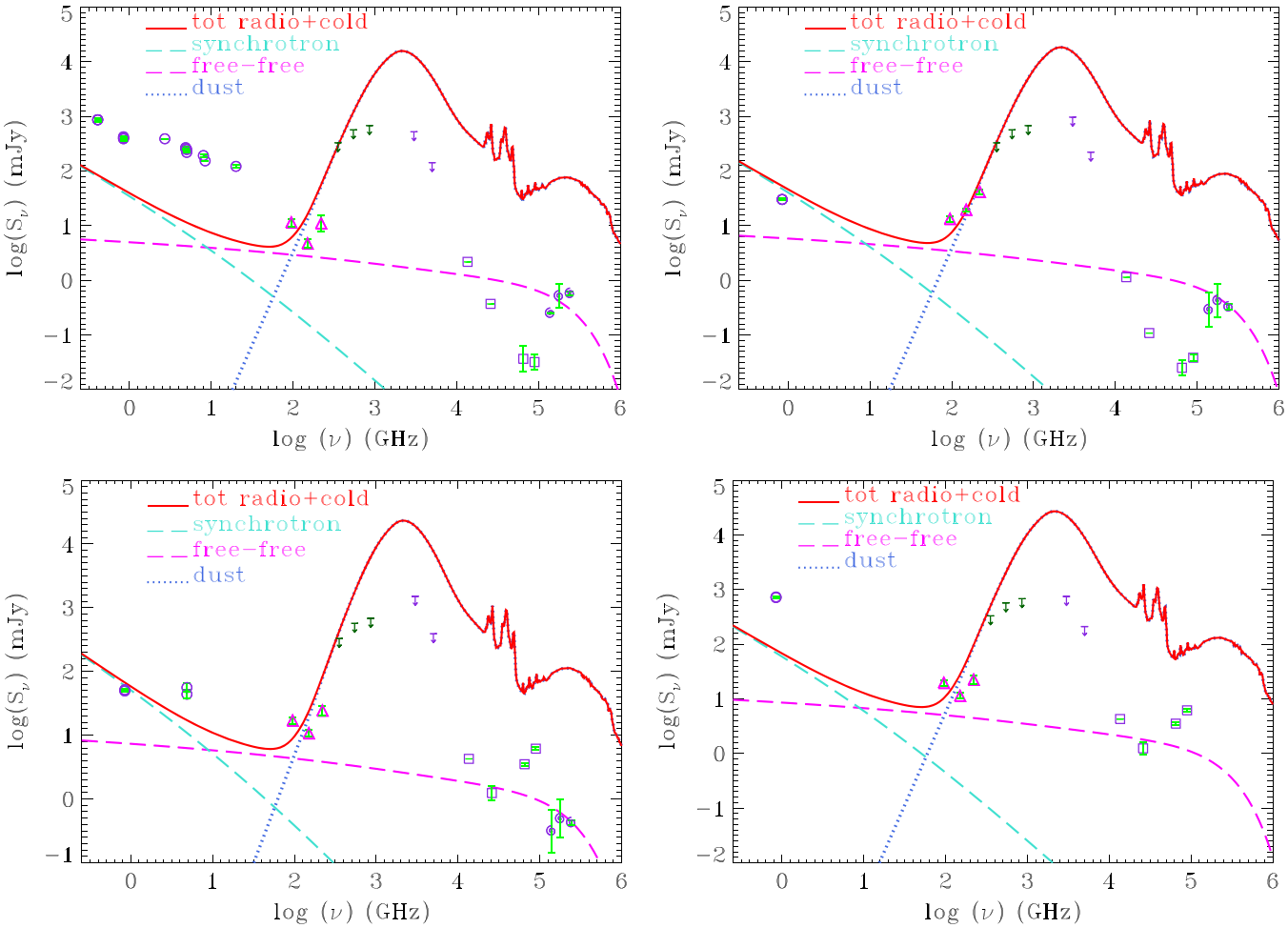

Figure 7. SPT sources selected at 95 GHz that have $1 > P(\alpha_{220}^{150} > 1.5) > 0.6$: SPT-SJ043651-5841-1 (top left), SPT-SJ203730-6513-3 (top right), SPT-SJ204101-5451-4 (bottom left), SPT-SJ213406-5334-3 (bottom right). Their SEDs are incompatible with those of star-forming galaxies, illustrated by the solid red line, and consistent with being radio sources. Data points: low-frequency radio flux densities from the NED (open circles); SPT flux densities (triangles); *WISE* flux densities (open squares); 2MASS flux densities (spirals); in violet and dark green are IRAS and *Planck* upper limits, respectively. We have adopted as *Planck* upper limits the 90% completeness limits of the *Planck* Catalog of Compact Sources (Planck Collaboration XXVIII et al. 2014) in the "extragalactic zone."

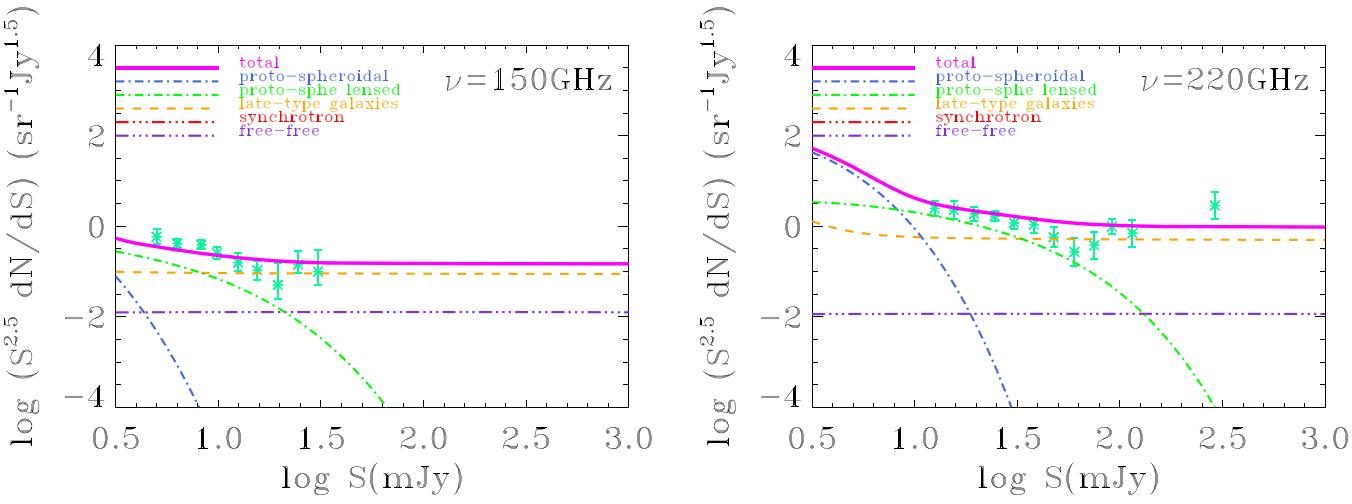

Figure 8. Euclidean normalized differential counts of dusty galaxies at 150 and at 220 GHz (left and right panels, respectively). The asterisks with error bars are the observational determinations by Mocanu et al. (2013). The various lines correspond to the contributions from the different emission processes and from the different galaxy populations, identified in the legend inside the panels. The lines corresponding to the synchrotron emission are below the lower limit of the *y*-axis. Note that in the considered flux density ranges the counts of star-forming galaxies seen via their radio emission are made by nearby sources and have thus an Euclidean slope. On the contrary, counts due to unlensed and lensed proto-spheroidal galaxies, seen via their dust emission, are due to strongly evolving high-*z* objects.

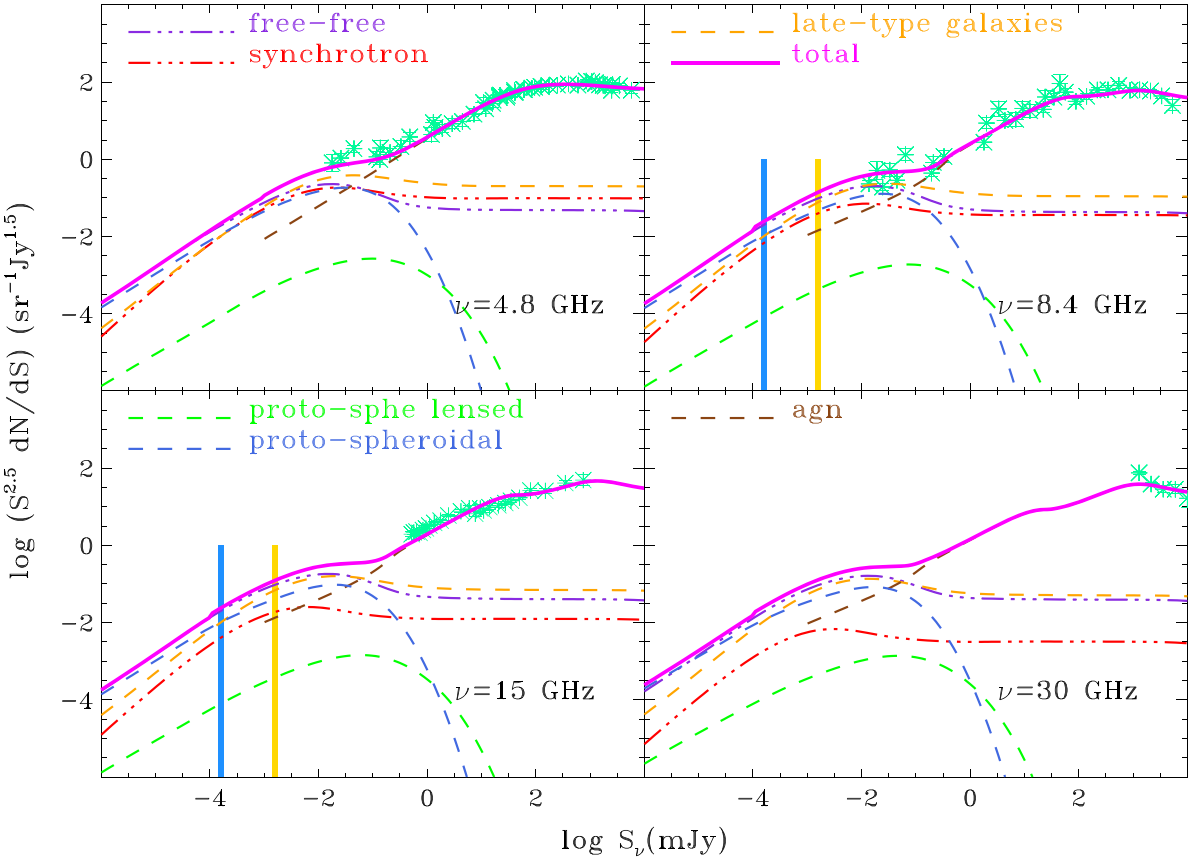

Figure 9. Predicted vs. observed counts at 4.8, 8.4, and 30 GHz. Dusty galaxies come up at sub-mJy flux density levels and their counts are accounted for by the model. At higher flux densities the counts are dominated by canonical, AGN-powered radio sources. The models shown are from Massardi et al. (2010) at 1.4, and 4.8 GHz and from de Zotti et al. (2005) at 8.4 and 30 GHz. The various lines correspond to the contributions from the different source populations (dashed yellow lines: late-type galaxies; dashed blue lines: unlensed proto-spheroidal galaxies; dashed green lines: strongly lensed proto-spheroidal galaxies; dashed brown lines: radio-loud AGNs; solid magenta line: total) and from the different emission processes (triple-dot dashed lines, red for synchrotron, violet for free–free). The solid vertical lines indicate the predicted flux density limits, for unresolved sources, of possible deep (yellow) and ultra-deep (blue) band 5 surveys with SKA1-MID.

survey instrument and has a very small field of view (the FWHM of the primary beam is 22″ at 300 GHz); however, it is interesting to compare its capabilities with the SKA (see Figure 12).

4.2. Strongly Lensed Galaxies

Figures 10 and 11 also show that a substantial fraction of the highest redshift galaxies that should be detected by the foreseen surveys are strongly lensed (magnification $\mu \geqslant 2$) proto-spheroids. The strongly lensed fraction at high z increases with increasing flux density limit, while the total counts rapidly decrease. Adopting the SISSA profile (Lapi et al. 2012) for the lens galaxies and an upper limit $\mu_{\rm max} = 30$ to the gravitational amplification, the model yields 1195, 432, 101, and 7.6 strongly lensed galaxies per square degree brighter than the SKA1-MID (band 2), the MIGHTEE and the EMU 5σ detection limits of 0.25, 1, 5, and 50 μJy, respectively (see Figure 13). They are approximately the 0.5%–0.6% of the total number of galaxies at these flux density limits (to be precise, the strongly lensed fractions are 0.62%, 0.52%, 0.47%, and 0.63%, respectively). The model with $\mu_{\rm max} = 30$ was shown by Bonato et al. (2014, their Figure 2) to provide a good fit to the SPT counts of dusty galaxies without an IRAS counterpart, interpreted as high-z strongly lensed galaxies. In the case of band 5 SKA1-MID surveys we predict, over the survey areas, $\simeq$4 and $\simeq$70 strongly lensed galaxies brighter than 0.15 and 1.5 μJy, respectively. They are about .36% of the total number of detected galaxies at both flux density limits.

To estimate the number of galaxies for which SKA1-MID can provide direct evidence of strong lensing by detecting at least two images we have turned to the classical Singular Isothermal Sphere (SIS) profile for lens galaxies, since the application of the SISSA model for this purpose is much more cumbersome. Details on the calculation are given in Appendix B. We find that two images will be detected for about 30% of strongly lensed galaxies brighter than 0.25 μJy at 1.4 GHz; this fraction decreases to about 20% at a flux limit of 5 μJy. This means that high-resolution radio observations alone will allow us to directly discern strong lensing for 20%–30% of the strongly lensed sources. Note that the detection of multiple images can happen thanks to the high spatial resolution of SKA1-MID surveys. It will not be generally possible with the lower resolution of EMU/ASKAP and MIGHTEE/MeerKAT surveys.

5. SYNERGIES WITH OPTICAL/SURVEYS

A full scientific exploitation of the data provided by the SKA surveys requires redshift determinations of the detected galaxies, especially of the most distant ones that can carry information on the earliest stages of galaxy formation. Several deep optical/near-IR imaging surveys covering substantial sky areas are ongoing or foreseen.

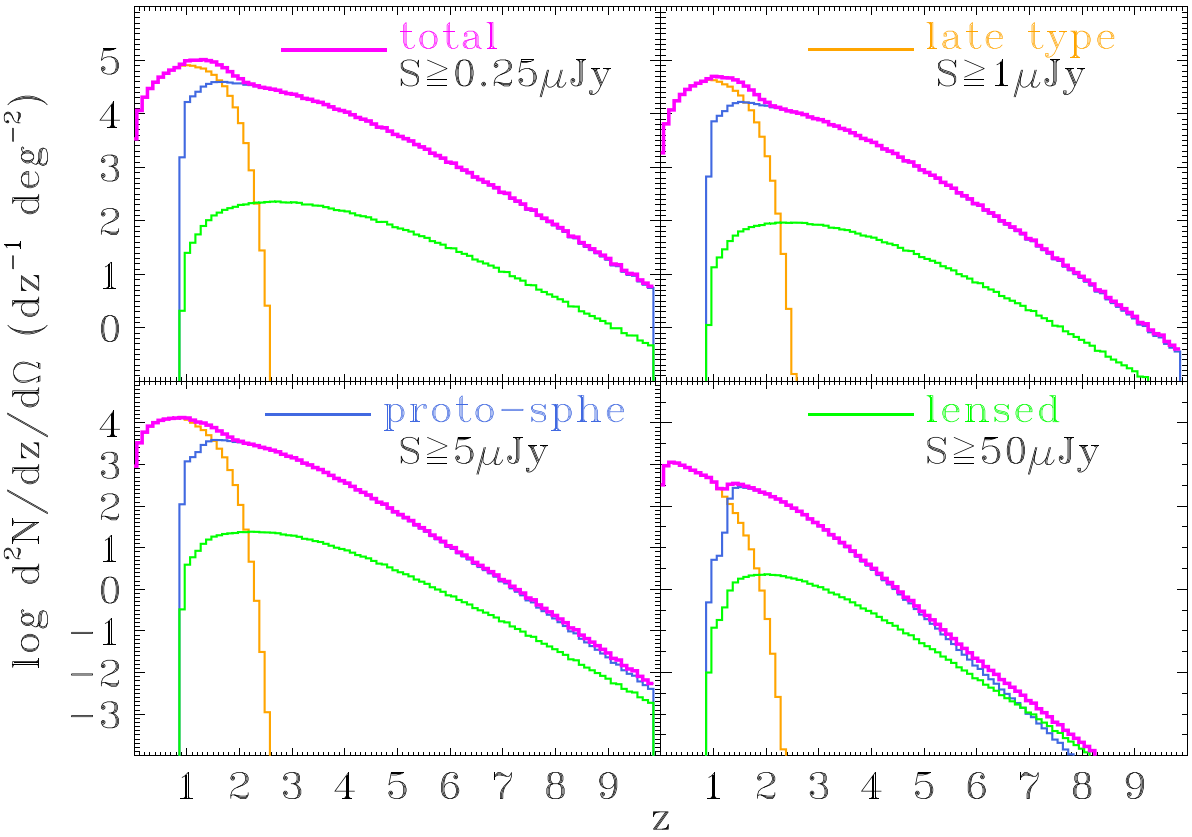

Figure 10. Predicted redshift distributions at the 5σ detection limits of the deepest SKA1-MID, of the MIGHTEE (MeerKAT) and of the EMU (ASKAP) 1.4 GHz surveys (see the text). The lines show the contributions of the various galaxy populations: late-type galaxies (yellow); unlensed proto-spheroidal galaxies (blue); strongly lensed proto-spheroidal galaxies (green); the magenta line shows the total.

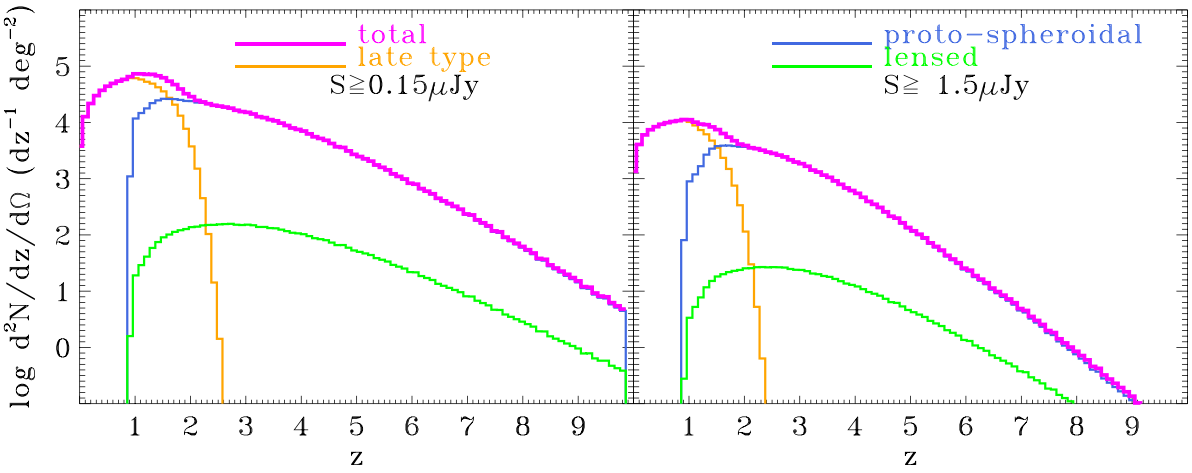

Figure 11. Predicted redshift distributions at the 5σ detection limits of SKA1-MID 10 GHz surveys (see the text). The lines show the contributions of the various galaxy populations: late-type galaxies (yellow); unlensed proto-spheroidal galaxies (blue); strongly lensed proto-spheroidal galaxies (green); the magenta line shows the total.

In Figure 14 we compare the minimum SFR of a dust-obscured galaxy (whose SED is shown in the right panel of Figure 15) detectable, as a function of redshift, by the deepest SKA1-MID survey with those detectable by the following surveys.

1. The *Euclid* deep survey covering an area of 40 deg^2 distributed over two fields close to the north and south ecliptic poles to 5σ magnitude limits for point source detection of 26 mag in the Y, H, and J bands and of 27.5 mag in the VIS (Laureijs et al. 2014).
2. The *Subaru* Hyper Suprime-Cam (HSC) ultra-deep survey[9] (Miyazaki et al. 2012) covering two fields of 1.8 deg^2, each to 5σ point source AB magnitude limits of $g = 28.1$, $r = 27.7$, $i = 27.4$, $z = 26.8$, and $y = 26.3$.
3. The four Large Synoptic Survey Telescope (LSST; Ivezic et al. 2008) deep drilling fields of 9.6 deg^2 each, aimed at reaching 5σ point source AB magnitude limits of 28 mag

[9] www.subarutelescope.org/Projects/HSC/surveyplan.html

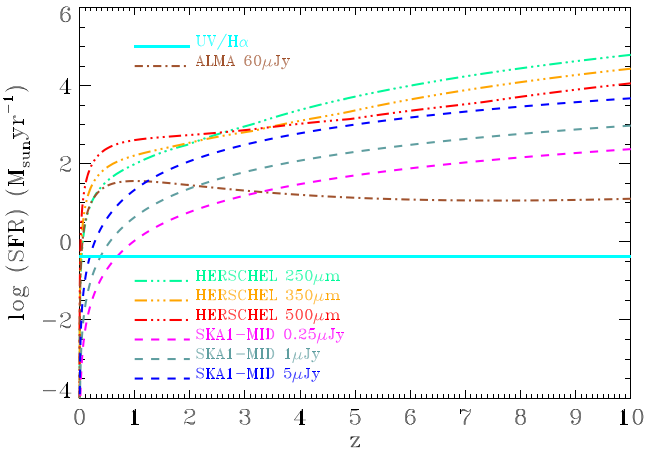

Figure 12. Minimum SFR detectable by SKA1-MID surveys 1.4 GHz down to 0.25 μJy (dashed magenta line), 1 μJy (dashed bottle green line), and 5 μJy (dashed blue line), as a function of z, compared with the minimum SFR detected by *Herschel*/SPIRE surveys, basically down to the confusion limits (dash–dot–dot–dotted lines, green for 250 μm, orange for 350 μm, and red for 500 μm) and by UV/Hα surveys (horizontal cyan line). The latter line corresponds to the average minimum absolute magnitude reached by the deepest surveys, which turns out to be almost independent of redshift. Note that while very deep in terms of SFR, the UV/Hα surveys miss the dust-enshrouded star formation. Also shown, for comparison, is the minimum SFR detectable in the deepest ALMA maps at 1.1 and 1.3 mm available so far (dot–dashed brown line; Carniani et al. 2015).

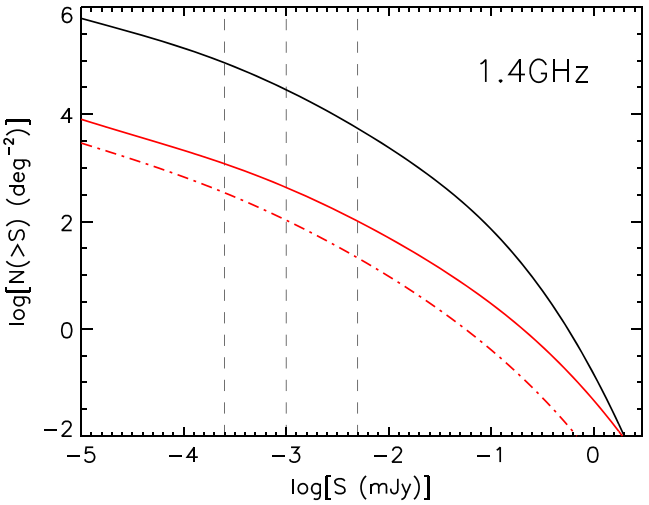

Figure 13. Predicted integral number counts of proto-spheroids at 1.4 GHz. The solid black curve represents the unlensed counts. The red curves represent the counts of strongly lensed galaxies as a function of the *total* (sum of all images) flux density (solid) and of the flux density of the fainter of the two images (dot–dashed). The vertical lines represent the three SKA1-MID 5σ detection limits for unresolved sources (i.e 0.25, 1, 5 μJy).

in the u, g, r, i , and z bands and of 26.8 in the y band (see Sect. 9.8 of the LSST Science Book[10]).

4. The Deep-Wide Survey (DWS; Windhorst et al. 2009) to be carried out with NIRCam on the *James Webb Space Telescope* (*JWST*). The DWS will image the sky with up to eight filters. A severe limitation to the exploitation of the SKA1-MID/DWS synergy is the smallness of the DWS area, 100 arcmin^2, i.e., a factor of $1/36 \simeq 0.028$ smaller than the area of the deepest SKA1-MID survey (1 deg^2). We expect that the SKA1-MID will detect, within the DWS area, $\simeq$6200 galaxies at $z \leqslant 6$ but only $\simeq$14 at $z \geqslant 6$.

The depth of the 4 LSST deep drilling fields is enough to detect all SKA1-MID dust-obscured galaxies in at least 3 bands up to $z \simeq 6$ and in at least one band up to $z \simeq 8$. Thus, photometric redshift estimates can be obtained up to $z \simeq 6$. With the obvious exception of the *JWST*/DWS the other surveys are somewhat less expedient. In the case of the UV-bright SED (left panel of Figure 15) all galaxies detected by the deepest SKA1-MID survey are easily detected by the above optical/near-IR surveys in all bands, so that accurate photometric redshift estimates can be obtained. Since, as argued above, strong dust obscuration appears to affect only a minority of faint $z \geqslant 6$ galaxies, it may be expected that photometric redshift estimates will be missing only for a small fraction of SKA1-MID high-z galaxies.

One may then wonder what the SKA1-MID adds to the information provided by deepest optical/near-IR surveys. Apart from the fact that the SFR inferred from SKA data are immune to the effect of dust obscuration, even in the case of no obscuration the SKA measurements are complementary to the optical/near-IR ones. As noted in section 3.1, while the rest-frame UV emission measures the instantaneous SFR, the synchrotron emission measures the SFR $\sim 10^7$ years earlier. Thus, in the absence of dust obscuration, the comparison of the SFR inferred from (rest-frame) UV photometry with that from low-frequency radio data, dominated by synchrotron, yields a measure of the starburst age (Clemens et al. 2008). Starbursts younger than $\sim 10^7$ years have a synchrotron emission decreasing with the starburst age, so that the inferred SFR is lower and lower than that inferred from UV data. By the same token, the comparison of SFRs derived from UV and low-frequency radio measurements is informative on variations of the SFR on timescales of $\sim 10^7$ years. A note of caution is in order, however. This comparison could not work at very high redshifts where the synchrotron emission may be highly suppressed due to the strong inverse Compton losses off the CMB (see Section 3.1 and, Carilli et al. 2008; Murphy 2009; Norris et al. 2013), so that even at relatively low frequencies the radio emission may not be synchrotron-dominated.

A rough redshift estimate for SKA1-MID galaxies missing better information can be obtained from the expected correlation of the radio spectral index with redshift. As z increases, the spectral index between the frequencies ν_1 and ν_2 in the observer frame, $\alpha = \log(S(\nu_1)/S(\nu_2))/\log(\nu_2/\nu_1)$, flattens with increasing z, due to the increasing contribution of free–free emission compared to synchrotron emission. As an example Figure 16 shows the redshift dependence of the spectral index between 1.4 and 4.8 GHz. The accurate photometric redshifts that can be provided by the optical/near-IR surveys will allow us to better assess this relation.

6. CONCLUSIONS

We have produced detailed predictions for the counts and the redshift distributions for planned surveys with the SKA1-MID and its precursors, taking into account the contributions of the different star-forming populations (late-type—normal and starburst—and proto-spheroidal galaxies), allowing for the effect of gravitational lensing. As mentioned in Section 2, the star formation is still ongoing in late-type galaxies, while it

[10] www.lsst.org/files/docs/sciencebook/SH_whole.pdf

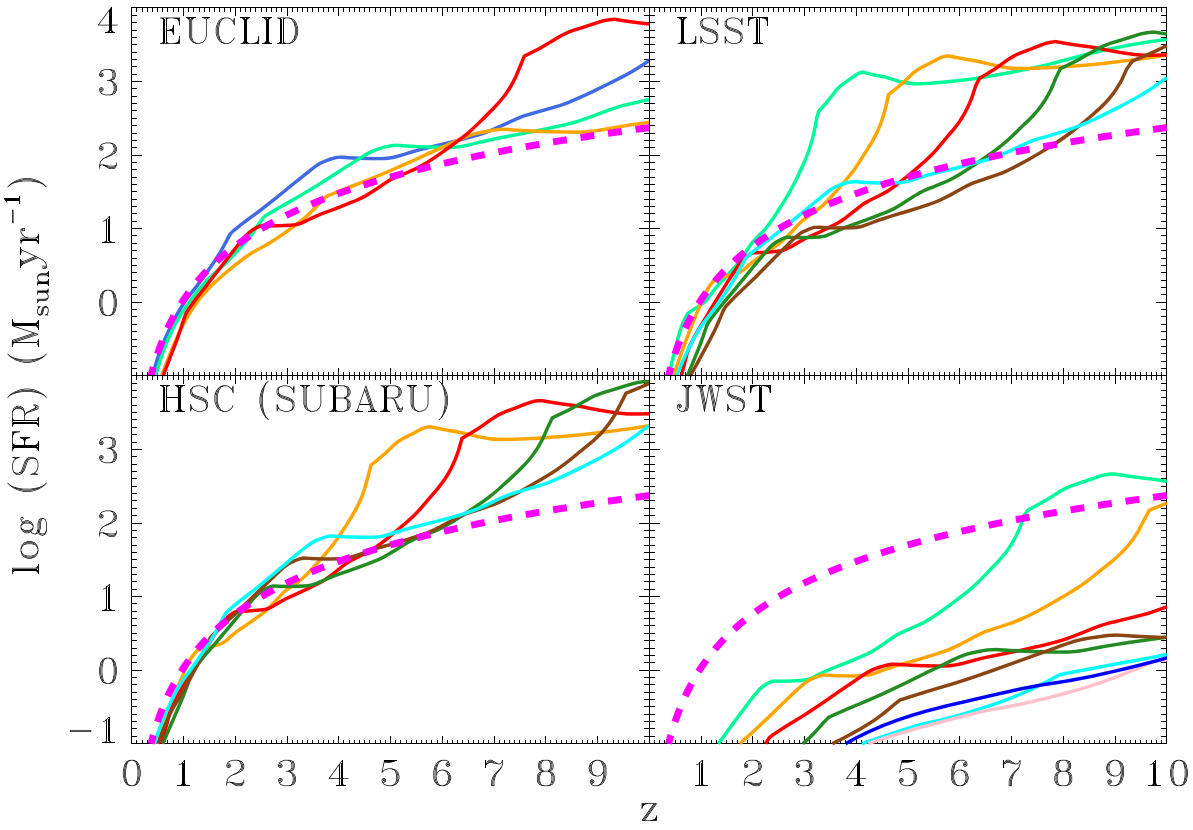

Figure 14. Minimum SFR detectable by the deepest SKA1-MID survey at 1.4 GHz (down to 0.25 μJy, dashed magenta line), compared with the minimum SFR detectable in each spectral band by the *Euclid* deep survey, by the *Subaru* HSC ultra-deep survey, by the LSST deep drilling fields and by the *JWST* DWS for the obscured SED shown in the right panel of Figure 15.

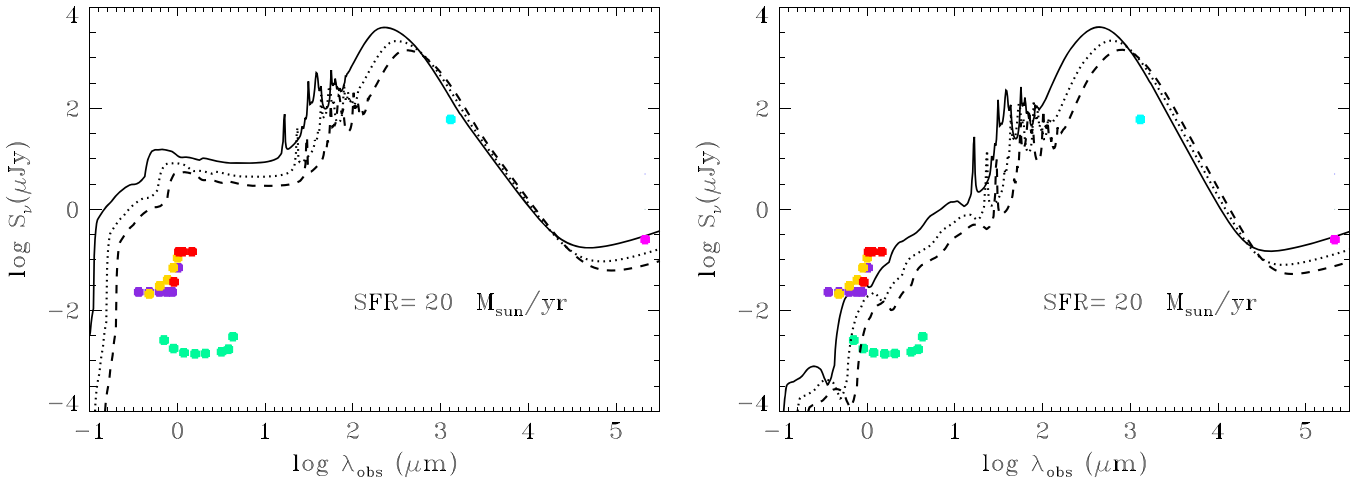

Figure 15. Left panel: detection limits of deep optical/near-IR surveys (left) and of the deepest SKA1-MID survey (magenta symbol on the right) compared with the spectral energy distribution of a UV-bright young galaxy with a SFR = 20 $M_\odot$ yr^{-1} at $z = 2$ (solid), 4 (dotted), and 6 (dashed). We have considered the following surveys (from top to bottom): *Euclid* deep (red), *Subaru* HSC ultra-deep (yellow), LSST deep drilling fields (violet), and *JWST* (green). The cyan point corresponds to the flux density limit of the deepest ALMA maps at 1.1 and 1.3 mm available so far (dotted–dashed brown line; Carniani et al. 2015). The SED was computed using the GRASIL package (Silva et al. 1998) for a Chabrier (2003) Initial Mass Function (IMF), a galaxy age of 10 Myr and a metallicity of 0.1 $Z_\odot$. Right panel: same as the left panel, but for an obscured SED with the same IMF and SFR, a Galactic age of 1 Gyr and a metallicity of 3 $Z_\odot$.

mostly occurred at $z \gtrsim 1.5$ in proto-spheroidal galaxies. Thus the dominant star-forming population gradually changes around $z \sim 1.5$. The predictions rely on the redshift evolution of the SFR function inferred from the wealth of data provided by surveys at far-IR to mm wavelengths as well as in the UV and in Hα. These data sets complement each other by probing the dust-obscured and unobscured star formation, respectively.

In practice, we have exploited the models by Cai et al. (2013) for the dust-obscured star formation and by Cai et al. (2014) for the total SFR function, including the unobscured one, at $z \gtrsim 2$. The missing contribution of the unobscured star formation at $z \lesssim 2$ has been added using a phenomenological approach. The model extended in this way has been further successfully tested against observational determinations at

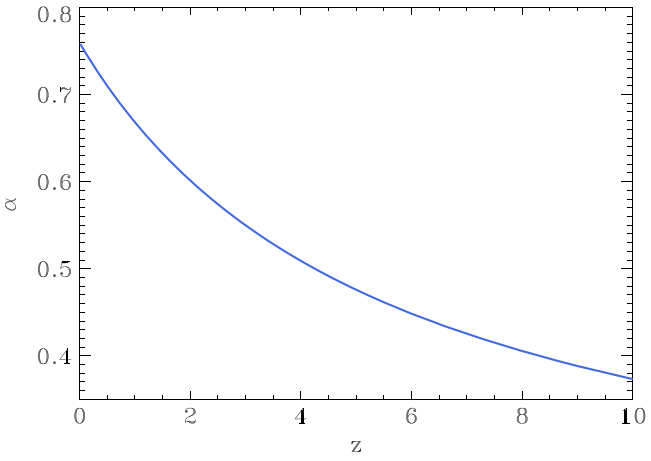

Figure 16. Spectral index between 1.4 and 4.8 GHz, α ($S_\nu \propto \nu^{-\alpha}$), in the observer frame, resulting from the combination of synchrotron and free–free emissions, as a function of z. The measured spectral index is thus a rough redshift indicator. Note, however, that the plotted curve does not take into account the possible increase of the synchrotron suppression in galaxies with increasing redshift due to inverse Compton scattering off of the CMB photons (see Section 3). This effect could hasten the convergence of the mean $\alpha(z)$ toward the free–free spectral index ($\alpha \simeq -0.1$) and introduce significant scatter especially at high z since this effect is highly dependent on how compact the star formation activity is within a system.

several redshifts of the Hα luminosity function, which is an independent measure of the SFR function.

The SFR functions were converted into radio luminosity functions, taking into account both the synchrotron and the free–free emissions, using the calibrations by Murphy et al. (2011, 2012). A comparison with the Mauch & Sadler (2007) local luminosity function for star-forming galaxies at 1.4 GHz showed evidence of a deviation from a linear relation between the SFR and the synchrotron luminosity, in the sense that low-SFR galaxies are under-luminous. This deviation was taken into account by means of a simple analytic formula. Good agreement with the bright portion of the luminosity function is achieved, adopting a dispersion of $\sigma_{\rm radio} = 0.4$ dex for the $L_{\rm radio}$–SFR relation.

This procedure, combined with the Massardi et al. (2010) model for radio-loud AGNs, allowed us to reproduce the available source counts in the range 1.4–30 GHz, but under-predicted the published SPT counts of dusty galaxies at 95 GHz (Mocanu et al. 2013). However, a careful reanalysis of the Mocanu et al. (2013) sample has shown that the surface density of dusty galaxies was appreciably overestimated. The revised counts are in very good agreement with model predictions, although the uncertainties are large, due to the poor statistics. Our reanalysis also showed that the main contribution to the observed 95 GHz flux density of local galaxies comes from free–free emission, not from thermal dust as implied by some models.

With the radio luminosity function in hand, radio-source counts and redshift distributions at the relevant frequencies and detection limits were straightforwardly computed. The highest redshift tails of the distributions at the detection limits of planned SKA1-MID surveys were found to include a substantial fraction of strongly lensed galaxies. We predict that a survey down to 0.25 μJy will detect about 1195 strongly lensed galaxies per square degree, at redshifts of up to 10. For about 30% of them the SKA1-MID can detect two images, thus providing direct evidence of strong lensing. The integral counts of strongly lensed galaxies are roughly proportional to $S^{-0.75}$ in the flux density range 0.01 μJy $< S_{1.4\,\rm GHz} <$ 1 μJy, implying that at fixed observing time, for the purpose of detecting these objects, it is more convenient to widen the covered area rather than going deeper. The counts substantially steepen above 10 μJy. Yet the EMU survey covering 30,000 deg^2 to a 50 μJy 5σ detection limit is expected to detect $\sim 2 \times 10^4$ strongly lensed galaxies.

The redshift distributions also show that the SKA1-MID surveys, and to some extent surveys with the SKA precursors, ASKAP and MeerKAT, will allow us to probe the star formation history through the re-ionization epoch without being affected by dust extinction. The deepest SKA1-MID surveys, down to 0.25 μJy, will extend the determination of the SFR function by about two orders of magnitude compared to *Herschel* surveys up to the highest redshifts.

Finally, we have discussed the synergies between the deepest SKA1 -MID survey and deep ongoing or planned optical/near-IR surveys. We find that the LSST deep drilling fields reach faint enough magnitudes to detect essentially all SKA1-MID galaxies in at least 3 bands, allowing reliable photometric redshift estimates. Exceptions may be heavily obscured $z > 6$ galaxies that are however expected to be rare. The *JWST*/DWS can detect also those in at least 6 filters, but its small area is a serious limitation.

We are indebted to R. Aversa for providing her analytic approximations for the redshift-dependent SFR functions and acknowledge constructive comments from the anonymous referee. This research has made use of the NASA/IPAC Extragalactic Database (NED), which is operated by the Jet Propulsion Laboratory, California Institute of Technology, under contract with the National Aeronautics and Space Administration, and of data products from the *Wide-field Infrared Survey Explorer*, which is a joint project of the University of California, Los Angeles, and the Jet Propulsion Laboratory/California Institute of Technology, funded by the National Aeronautics and Space Administration. We acknowledge financial support from ASI/INAF Agreement 2014-024-R.0 for the *Planck* LFI activity of Phase E2, from PRIN INAF 2012, project "Looking into the dust-obscured phase of galaxy formation through cosmic zoom lenses in the *Herschel* Astrophysical Large Area Survey" and from PRIN INAF 2014, project "Probing the AGN/galaxy co-evolution through ultra-deep and ultra-high-resolution radio surveys." Z.Y.C. is supported by China Postdoctoral Science Foundation No. 2014M560515. A. L. thanks SISSA for warm hospitality.

APPENDIX A
EVOLUTION OF THE UV AND Hα LUMINOSITY FUNCTIONS OF LATE-TYPE GALAXIES

For the UV ($\lambda = 1500$ Å) luminosity functions of late-type galaxies we adopted the functional form chosen by Cai et al. (2013) for the IR luminosity function of these galaxies:

$$\Phi(\log L_{1500}, z) d \log L_{1500} = \Phi^* \left(\frac{L_{1500}}{L^*} \right)^{1-\alpha} \times \exp\left[-\frac{\log^2(1 + L_{1500}/L^*)}{2\sigma^2} \right] d \log L_{1500}. \quad (10)$$

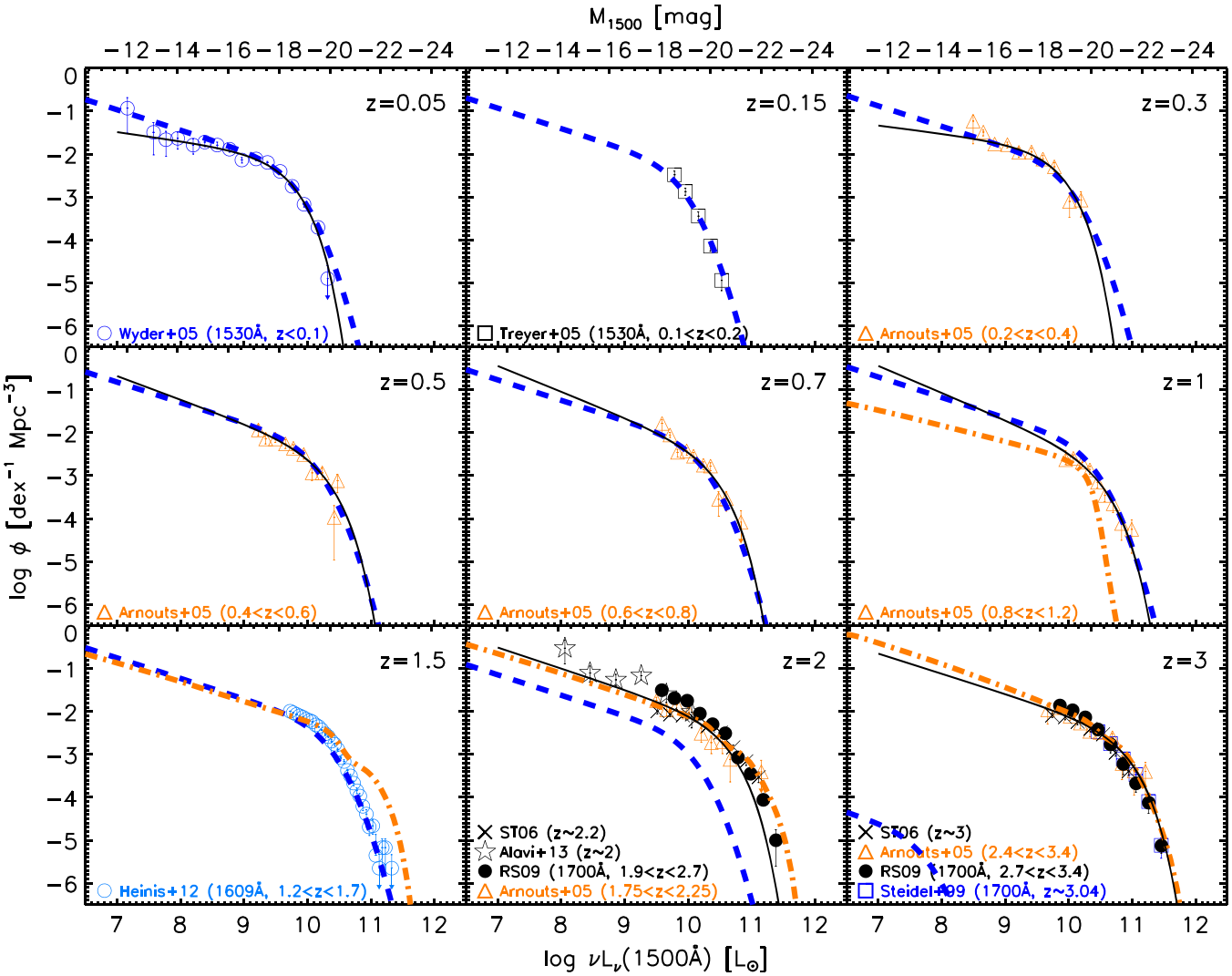

Figure 17. Comparison of the observed 1500 Å luminosity functions at several redshifts with the model described in the text. The dashed blue lines correspond to the pure luminosity evolution model for late-type galaxies. The contribution of proto-spheroidal galaxies (dotted–dashed orange lines) begins to show up at $z \simeq 1.5$ and becomes dominant at higher redshifts. This contribution was obtained from the 1350 Å luminosity functions computed by Cai et al. (2014) assuming a flat intrinsic UV spectrum [e.g., $L_\nu(1500\,\text{Å}) = L_\nu(1350\,\text{Å})$] and a Calzetti et al. (2000) extinction curve, yielding $A_{1500} = A_{1350} \times k(1500\,\text{Å})/k(1350\,\text{Å}) = 0.936A_{1350}$. The data at different UV wavelengths have been brought to 1500 Å in an analogous way. In some panels we also show, for comparison, the model by Arnouts et al. (2005, thin solid black lines). The data are from Arnouts et al. (2005), Treyer et al. (2005), Wyder et al. (2005), Sawicki & Thompson (2006, ST06), Reddy & Steidel (2009, RS09), Heinis et al. (2013); and Alavi et al. (2014).

We obtained a sufficiently good description of the data using a simple pure luminosity evolution model [$L^*(z) = L_0^*(1+z)^{\alpha_L}$ up to $z = 1$; see Figure 17]. The best-fit values of the parameters are $\log[\Phi_0^*(\text{dex}^{-1}\,\text{Mpc}^{-3})] = -2.150 \pm 0.095$, $\log(L_0^*/L_\odot) = 9.436 \pm 0.119$, $\alpha = 1.477 \pm 0.050$, $\sigma = 0.326 \pm 0.035$, and $\alpha_L = 2.025 \pm 0.063$. The free parameters are constrained using the data at $z \leqslant 1$ by Wyder et al. (2005), Treyer et al. (2005), and Arnouts et al. (2005). In Figure 17 the thin solid black lines show, for comparison, the Schechter fits by Arnouts et al. (2005). The dot–dashed orange lines show the contributions of proto-spheroidal galaxies derived adopting $A_{1500} = A_{1350} \cdot k(1500\,\text{Å})/k(1350\,\text{Å}) = 0.936A_{1350}$ (Calzetti et al. 2000).

As argued by Hopkins et al. (2001), dust reddening of late-type galaxies appears to be dependent on the SFR. Adopting their relation and the Calzetti et al. (2000) extinction law, the extinction of the Hα line is given by:

$$A_{\text{H}\alpha}(\text{logSFR}) = 6.536 \log\left[\frac{0.797\,\log(\text{SFR}) + 3.834}{2.88}\right]. \quad (11)$$

The corresponding UV extinction at 1500 Å, based on the Calzetti et al. (2000) law, is

$$A_{1500} = \frac{k(1500\,\text{Å})}{k(6563\,\text{Å})}\frac{E(B-V)_{\text{star}}}{E(B-V)_{\text{gas}}}A_{\text{H}\alpha} = 3.107 \times 0.44 \times A_{\text{H}\alpha} = 1.367A_{\text{H}\alpha}, \quad (12)$$

where we have taken into account that the color excess appropriate for the stellar continuum, $E(B-V)_{\text{star}}$, is related to that for nebular gas emission lines, $E(B-V)_{\text{gas}}$, by $E(B-V)_{\text{star}} = 0.44E(B-V)_{\text{gas}}$ (Calzetti et al. 2000).

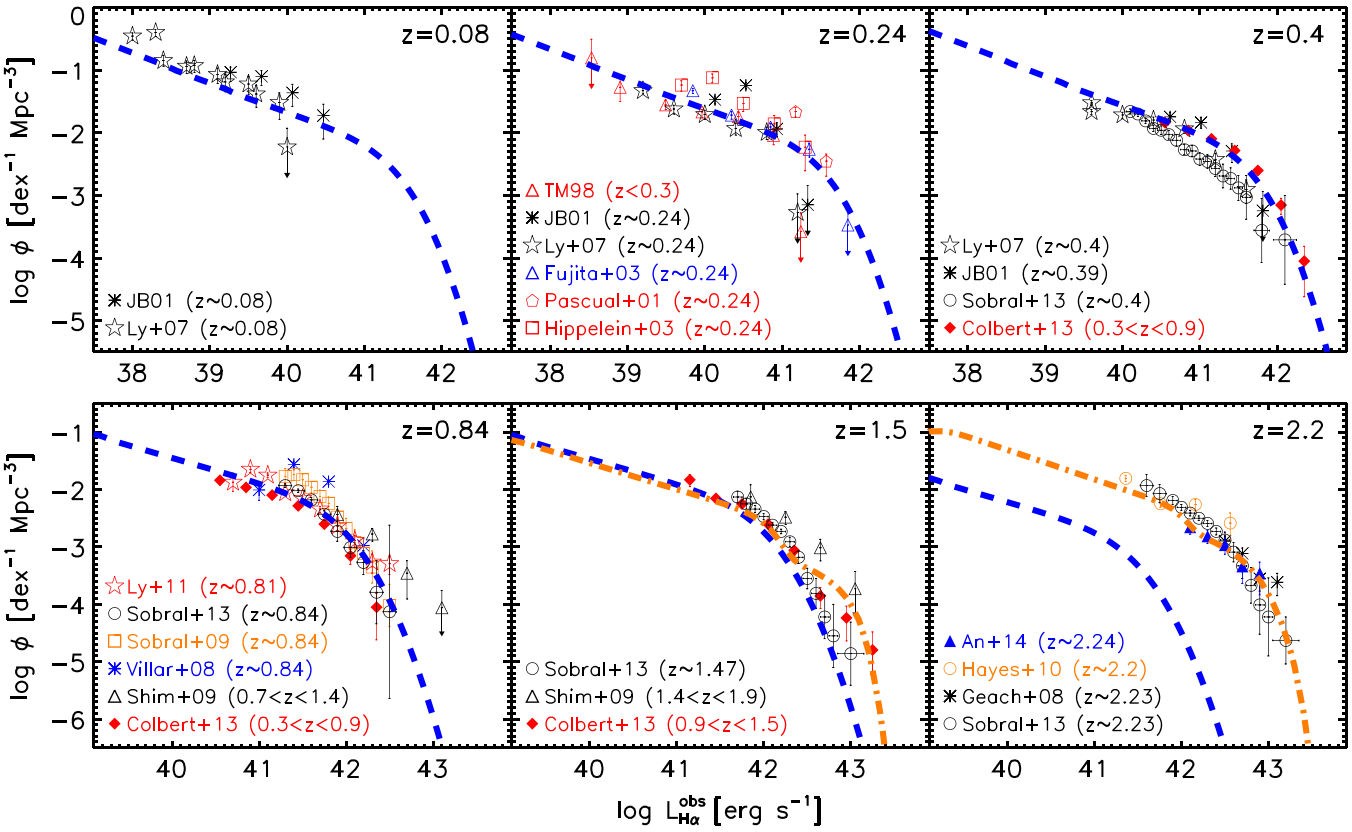

Figure 18. Comparison of the observed Hα luminosity functions not corrected for dust attenuation with those yielded by the model, attenuated as described in the text. The dashed blue lines are for the UV-bright late-type galaxies and the dot–dashed orange lines are for proto-spheroids.

The UV luminosity functions of late-type galaxies have been corrected for the SFR-dependent dust extinction and converted into SFR functions using the Kennicutt & Evans (2012) calibration

$$\log\left(\frac{L_{1500}}{L_{\odot}}\right) = \log\left(\frac{\mathrm{SFR}}{M_{\odot}\ \mathrm{yr}^{-1}}\right) + 9.825 - 0.4A_{1500}(\log\mathrm{SFR}), \quad (13)$$

via the equation

$$\frac{d^2N(\log\mathrm{SFR})}{d\log\mathrm{SFR}dV} = \frac{d^2N(\log L_{1500})}{d\log L_{1500}dV}\cdot\frac{d\log L_{1500}}{d\log\mathrm{SFR}} = \frac{d^2N(\log L_{1500})}{d\log L_{1500}dV}\cdot\left[1 - 0.4\frac{dA_{1500}}{d\log\mathrm{SFR}}\right]. \quad (14)$$

The results are shown in Figure 1. As a further test of the model we have used the SFR functions obtained combining UV and IR data to derive the Hα luminosity functions at several redshifts, adopting the Kennicutt & Evans (2012) calibration. To compare them with observations we have applied the SFR-dependent dust attenuation of Equation (11) in the case of late-type galaxies and the Calzetti relation between Hα and UV extinction in the case of proto-spheroids:

$$A_{\mathrm{H}\alpha} = \frac{k(6563\ \text{Å})}{k(1350\ \text{Å})}\frac{E(B-V)_{\mathrm{gas}}}{E(B-V)_{\mathrm{ste}}}$$
$$A_{1350} = \frac{3.3258}{11.039}\frac{1}{0.44}A_{1350} = 0.685A_{1350}. \quad (15)$$

As shown by Figure 18, the agreement is generally good, with a hint that Hα surveys may miss galaxies with the highest SFRs, particularly at $z \simeq 1.5$. Figure 1 shows that SFR estimates from Hα luminosities exceed those from UV luminosities if both are uncorrected for dust attenuation, consistent with the lower attenuation at the Hα compared to UV wavelengths (Equation (15)).

APPENDIX B
COUNTS OF STRONGLY LENSED SOURCES

In a SIS model the strong lensing regime (i.e., the formation of multiple images) corresponds to $\mu_{\mathrm{tot}} \geqslant 2$, where μ_{tot} is the *total* amplification, which is the sum of the modules of the amplifications of the two images. In fact, in a SIS model, two (and only two) images can form in the strong lensing regime. If we indicate with μ_+ and μ_- the values of the amplifications of the two images we find

$$\mu_+ = \frac{\beta + \theta_{\mathrm{E}}}{\beta} > 0 \quad (16)$$

$$\mu_- = \frac{\beta - \theta_{\mathrm{E}}}{\beta} < 0, \quad (17)$$

where β is the angular separation of the background source from the optical axis of the lens system. In the strong lensing regime $\beta < \theta_{\mathrm{E}}$, θ_{E} is the Einstein radius

$$\theta_{\mathrm{E}} = 4\pi\left(\frac{\sigma_v}{c}\right)^2\frac{D_{\mathrm{LS}}}{D_{\mathrm{S}}}. \quad (18)$$

Here σ_v is the one-dimensional (1D) velocity dispersion of the lens, D_S is the angular diameter distance to the source, and D_{LS} is the angular diameter distance from the lens to the source. From the above equations it follows that

$$\mu_{tot} = \mu_+ + |\mu_-| = \frac{2\theta_E}{\beta}. \quad (19)$$

It is worth noticing that the strong lensing regime implies $\beta \leqslant \theta_E$ and, therefore $\mu_+ \geqslant 2$ and $|\mu_-| \geqslant 0$.

The cross-section for strong lensing with total amplification higher than a given value $\mu_{tot} \geqslant 2$ is

$$\Sigma(\geqslant \mu_{tot}) = \pi \frac{4\theta_E^2}{\mu_{tot}^2}. \quad (20)$$

Similarly, the cross section for strong lensing with the second image (the fainter one) with the module of the amplification higher than a given value $|\mu-|$ is

$$\Sigma(\geqslant |\mu_-|) = \pi \frac{\theta_E^2}{(1+|\mu_-|)^2}. \quad (21)$$

Once the lensing cross-section is known, the corresponding probability is given by (in the "non-overlapping" cross-section's approximation, i.e., neglecting lensing by more than one foreground mass; Peacock 1982)

$$P(>\mu|z_S) = \int_{z_L^{min}}^{z_L^{max}} \int_{M_L^{min}}^{M_L^{max}} \Sigma(>\mu|M_L, z_L, z_S) \times \frac{d^2N_L}{dM_L dz_L} dM_L dz_L, \quad (22)$$

where z_S and z_L are the redshifts of the background source and of the lens, respectively, while $d^2N_L/dM_L dz_L$ is the number density of lenses per unit mass and redshift interval. The usual choice for the mass distribution of the lenses is the mass function of the dark matter halos derived from N-body simulations (e.g., Sheth & Tormen 1999).

The halo mass is related to θ_E (and therefore to the the lensing cross-section) via the 1D velocity dispersion of the lens, σ_v, by

$$\sigma_v^2 = \frac{GM_L}{2R_{L,vir}} \quad (23)$$

where $R_{L,vir}$ is the virial radius of the lens that we compute assuming a virialization redshift $z_{L,vir} = 2.5$ (see Lapi et al. 2012).

Given the *true* number density of unlensed sources per unit logarithmic interval in flux density and per unit interval in redshift, $(d^2N/d\log S\, dz)_T$, the corresponding number density of lensed sources is computed as

$$\left[\frac{d^2N(S, z_S)}{d\log S\, dz_S}\right]_L = \int_{\mu_{min}}^{\mu_{max}} \left[\frac{d^2N(S/\mu, z_S)}{d\log S dz_S}\right]_T \times p(\mu|z_S) d\mu, \quad (24)$$

where S is the *measured* flux density of the sources and $p(\mu|z_S)d\mu$ is the probability that a source at redshift z_S has its flux density boosted by a factor μ, within $d\mu$, because of a lensing event. This probability is obtained from Equation (22) as $p(\mu|z_S) = -dP(>\mu|z_S)/d\mu$. The upper integration limit, μ_{max}, is set by the size of the background source, with $\mu_{tot,max} = \infty$ for a point source.

The solid and the dashed red curves in Figure 13 have been derived by plugging into Equation (22) the lensing cross-sections given by Equations (20) and (21), respectively, and assuming in both cases that $\mu_{tot,max} = 30$ (translating to $|\mu_-| \leqslant \mu_{tot,max}/2 - 1 = 14$).

REFERENCES

Alavi, A., Siana, B., Richard, J., et al. 2014, ApJ, 143, 780
Amblard, A., Cooray, A., Serra, P., et al. 2011, Natur, 470, 510
Arnouts, S., Schiminovich, D., Ilbert, O., et al. 2005, ApJL, 619, L43
Aversa, R., Lapi, A., de Zotti, G., Shankar, F., & Danese, L. 2015, ApJ, in press (arXiv:1507.07318)
Banday, A. J., & Wolfendale, A. W. 1991, MNRAS, 248, 705
Baugh, C. M., Lacey, C. G., Frenk, C. S., et al. 2005, MNRAS, 356, 1191
Bell, E. F. 2003, ApJ, 586, 794
Bernardi, M., Shankar, F., Hyde, J. B., et al. 2010, MNRAS, 404, 2087
Béthermin, M., Dole, H., Lagache, G., Le Borgne, D., & Penin, A. 2011, A&A, 529, A4
Bonato, M., Negrello, M., Cai, Z.-Y., et al. 2014, MNRAS, 438, 2547
Bonzini, M., Padovani, P., Mainieri, V., et al. 2013, MNRAS, 436, 3759
Bourne, N., Dunne, L., Ivison, R. J., et al. 2011, MNRAS, 410, 1155
Bouwens, R. J., Illingworth, G. D., Franx, M., & Ford, H. 2008, ApJ, 686, 230
Bouwens, R. J., Illingworth, G. D., Labbe, I., et al. 2011a, Natur, 469, 504
Bouwens, R. J., Illingworth, G. D., Oesch, P. A., et al. 2011b, ApJ, 737, 90
Bouwens, R. J., Oesch, P. A., Labbe, I., et al. 2015, arXiv:1506.01035
Burgarella, D., Buat, V., Gruppioni, C., et al. 2013, A&A, 554, A70
Cai, Z.-Y., Lapi, A., Bressan, A., et al. 2014, ApJ, 785, 65
Cai, Z.-Y., Lapi, A., Xia, J.-Q., et al. 2013, ApJ, 768, 21
Calzetti, D., Armus, L., Bohlin, R. C., et al. 2000, ApJ, 533, 682
Capak, P. L., Carilli, C., Jones, G., et al. 2015, Natur, 522, 455
Caputi, K. I., Lagache, G., Yan, L., et al. 2007, ApJ, 660, 97
Carilli, C. L., Lee, N., Capack, P., et al. 2008, ApJ, 689, 883
Carniani, S., Maiolino, R., De Zotti, G., et al. 2015, arXiv:1502.00640
Chabrier, G. 2003, PASP, 115, 763
Chi, X., & Wolfendale, A. W. 1990, MNRAS, 245, 101
Chomiuk, L., & Povich, M. S. 2011, AJ, 142, 197
Clemens, M. S., Negrello, M., De Zotti, G., et al. 2013, MNRAS, 433, 695
Clemens, M. S., Vega, O., Bressan, A., et al. 2008, A&A, 477, 95
Condon, J. J. 1992, ARA&A, 30, 575
Condon, J. J., Cotton, W. D., Fomalont, E. B., et al. 2012, ApJ, 758, 23
Condon, J. J., Helou, G., & Jarrett, T. H. 2002, AJ, 123, 1881
Cooray, A., Amblard, A., Wang, L., et al. 2010, A&A, 518, L22
Davé, R., Oppenheimer, B. D., Katz, N., Kollmeier, J. A., & Weinberg, D. H. 2010, MNRAS, 408, 2051
de Zotti, G., Massardi, M., Negrello, M., & Wall, J. 2010, A&ARv, 18, 1
de Zotti, G., Ricci, R., Mesa, D., et al. 2005, A&A, 431, 893
Draine, B. T. 2011, Physics of the Interstellar and Intergalactic Medium (Princeton, NJ: Princeton Univ. Press)
Draine, B. T., & Lazarian, A. 1998, ApJL, 494, L19
Fujita, S. S., Ajiki, M., Shioya, Y., et al. 2003, ApJL, 586, L115
Garn, T., & Best, P. N. 2010, MNRAS, 409, 421
Garn, T., Sobral, D., Best, P. N., et al. 2010, MNRAS, 402, 2017
Geach, J. E., Smail, I., Best, P. N., et al. 2008, MNRAS, 388, 1473
Granato, G. L., De Zotti, G., Silva, L., Bressan, A., & Danese, L. 2004, ApJ, 600, 580
Gruppioni, C., Pozzi, F., Rodighiero, G., et al. 2013, MNRAS, 432, 23
Hayes, M., Schaerer, D., & Östlin, G. 2010, A&A, 509, L5
Heinis, S., Buat, V., Béthermin, M., et al. 2013, MNRAS, 429, 1113
Helou, G., Soifer, B. T., & Rowan-Robinson, M. 1985, ApJL, 298, L7
Hibon, P., Cuby, J.-G., Willis, J., et al. 2010, A&A, 515, 97
Hippelein, H., Maier, C., Meisenheimer, K., et al. 2003, A&A, 402, 65
Hopkins, A. M., Connolly, A. J., Haarsma, D. B., & Cram, L. E. 2001, AJ, 122, 288
Ivezic, Z., Tyson, J. A., Abel, B., et al. 2008, arXiv:0805.2366
Ivison, R. J., Magnelli, B., Ibar, E., et al. 2010, A&A, 518, L31
Iye, M., Ota, K., Kashikawa, N., et al. 2006, Natur, 443, 186
Jarvis, M. J., Smith, D. J. B., Bonfield, D. G., et al. 2010, MNRAS, 409, 92
Jiang, L., Bian, F., Fan, X., et al. 2013, ApJL, 771, L6
Jones, D. H., & Bland-Hawthorn, J. 2001, ApJ, 550, 593
Kennicutt, R. C., & Evans, N. J. 2012, ARA&A, 50, 531

Klein, U., Wielebinski, R., & Thuan, T. X. 1984, A&A, 141, 241
Kroupa, P. 2001, MNRAS, 322, 231
Lacey, C. G., Baugh, C. M., Frenk, C. S., et al. 2010, MNRAS, 405, 2
Lacki, B. C., Thompson, T. A., & Quataert, E. 2010, ApJ, 717, 1
Lapi, A., & Cavaliere, A. 2011, ApJ, 743, 127
Lapi, A., González-Nuevo, J., Fan, L., et al. 2011, ApJ, 742, 24
Lapi, A., Negrello, M., González-Nuevo, J., Cai, Z.-Y., et al. 2012, ApJ, 755, 46
Lapi, A., Raimundo, S., Aversa, R., et al. 2014, ApJ, 782, 69
Lapi, A., Shankar, F., Mao, J., et al. 2006, ApJ, 650, 42
Laureijs, R., Hoar, J., Buenadicha, G., et al. 2014, adass XXIII, 485, 495
Leitherer, C., Schaerer, D., Goldader, J. D., et al. 1999, ApJS, 123, 3
Ly, C., Lee, J. C., Dale, D. A., et al. 2011, ApJ, 726, 109
Ly, C., Malkan, M. A., Kashikawa, N., et al. 2007, ApJ, 657, 738
Ly, C., Malkan, M. A., Kashikawa, N., et al. 2012, ApJL, 747, L16
Madau, P., & Dickinson, M. 2014, ARA&A, 52, 415
Maddox, S. J., Dunne, L., Rigby, E., et al. 2010, A&A, 518, L11
Magnelli, B., Elbaz, D., Chary, R. R., et al. 2011, A&A, 528, A35
Magnelli, B., Popesso, P., Berta, S., et al. 2013, A&A, 553, A132
Mancini, M., Schneider, R., Graziani, L., et al. 2015, arXiv:1505.01841
Mao, J., Lapi, A., Granato, G. L., de Zotti, G., & Danese, L. 2007, ApJ, 667, 655
Mao, M. Y., Huynh, M. T., Norris, R. P., et al. 2011, ApJ, 731, 79
Massardi, M., Bonaldi, A., Negrello, M., et al. 2010, MNRAS, 404, 532
Mauch, T., & Sadler, E. M. 2007, MNRAS, 375, 931
McLure, R. J., Dunlop, J. S., Bowler, R. A. A., et al. 2013, MNRAS, 432, 2696
Mitchell, K. J., & Condon, J. J. 1985, AJ, 90, 1957
Miyazaki, S., Komiyama, Y., Nakaya, H., et al. 2012, Proc. SPIE, 8446, 84460Z
Mocanu, L. M., Crawford, T. M., Vieira, J. D., et al. 2013, ApJ, 779, 61
Muñoz, J. A., & Loeb, A. 2011, ApJ, 729, 99
Murphy, E. J. 2009, ApJ, 706, 482
Murphy, E. J. 2013, ApJ, 777, 58
Murphy, E. J., Bremseth, J., Mason, B. S., et al. 2012, ApJ, 761, 97
Murphy, E. J., Condon, J. J., Schinnerer, E., et al. 2011, ApJ, 737, 67
Murphy, E. J., Sargent, M. T., Beswick, R. J., et al. 2015, PoS(AASKA14)085
Norris, R. P., Afonso, J., Bacon, D., et al. 2013, PASA, 30, 20
Norris, R. P., Hopkins, A. M., Afonso, J., et al. 2011, PASA, 28, 215
Oesch, P. A., Bouwens, R. J., Illingworth, G. D., et al. 2012, ApJ, 759, 135
Oesch, P. A., Bouwens, R. J., Illingworth, G. D., et al. 2013, ApJ, 773, 75
Oesch, P. A., Bouwens, R. J., Illingworth, G. D., et al. 2014, ApJ, 786, 108
Ota, K., Iye, M., Kashikawa, N., et al. 2008, ApJ, 677, 12
Ota, K., Iye, M., Kashikawa, N., et al. 2010, ApJ, 722, 803
Owen, F. N., & Morrison, G. E. 2008, AJ, 136, 1889
Padovani, P., Bonzini, M., Miller, N., et al. 2014, IAU Symp. 304, Multiwavelength AGN Surveys and Studies (Cambridge: Cambridge Univ. Press), 79
Padovani, P., Miller, N., Kellermann, K. I., et al. 2011, ApJ, 740, 20
Pascual, S., Gallego, J., Aragón-Salamanca, A., & Zamorano, J. 2001, A&A, 379, 798
Peacock, J. A. 1982, MNRAS, 199, 987
Planck Collaboration XVI, Ade, P. A. R., Aghanim, N., et al. 2014, A&A, 571, A16
Planck Collaboration XVIII, Ade, P. A. R., Aghanim, N., et al. 2011, A&A, 536, A18
Planck Collaboration XX, Ade, P. A. R., Aghanim, N., et al. 2011, A&A, 536, A20
Planck Collaboration XXV, Ade, P. A. R., Aghanim, N., et al. 2014, arXiv:1407.5452
Planck Collaboration XXVIII, Ade, P. A. R., Aghanim, N., et al. 2014, A&A, 571, A28
Planck Collaboration XXX, Ade, P. A. R., Aghanim, N., et al. 2014, A&A, 571, A30
Prandoni, I., & Seymour, N. 2014, arXiv:1412.6942
Price, R., & Duric, N. 1992, ApJ, 401, 81
Reddy, N., Dickinson, M., Elbaz, D., et al. 2012, ApJ, 744, 154
Reddy, N. A., & Steidel, C. C. 2009, ApJ, 692, 778
Riechers, D. A., Bradford, C. M., Clements, D. L., et al. 2013, Natur, 496, 329
Rodighiero, G., Vaccari, M., Franceschini, A., et al. 2010, A&A, 515, A8
Romano, D., Silva, L., Matteucci, F., & Danese, L. 2002, MNRAS, 334, 444
Sawicki, M., & Thompson, D. 2006, ApJ, 642, 653
Schenker, M. A., Robertson, B. E., Ellis, R. S., et al. 2013, ApJ, 768, 196
Sheth, R. K., & Tormen, G. 1999, MNRAS, 308, 119
Shibuya, T., Kashikawa, N., Ota, K., et al. 2012, ApJ, 752, 114
Silva, L., Granato, G. L., Bressan, A., & Danese, L. 1998, ApJ, 509, 103
Smit, R., Bouwens, R. J., Franx, M., et al. 2012, ApJ, 756, 14
Sobral, D., Best, P. N., Geach, J. E., et al. 2009, MNRAS, 398, 75
Sobral, D., Smail, I., Best, P. N., et al. 2013, MNRAS, 428, 1128
Steidel, C. C., Adelberger, K. L., Giavalisco, M., Dickinson, M., & Pettini, M. 1999, ApJ, 519, 1
Sullivan, M., Mobasher, B., Chan, B., et al. 2001, ApJ, 558, 72
Tresse, L., & Maddox, S. J. 1998, ApJ, 495, 691
Treyer, M., Wyder, T. K., Schiminovich, D., et al. 2005, ApJL, 619, L19
Vernstrom, T., Scott, D., Wall, J. V., et al. 2014, MNRAS, 440, 2791
Viero, M. P., Wang, L., Zemcov, M., et al. 2013, ApJ, 772, 77
Villar, V., Gallego, J., Pérez-González, P. G., et al. 2008, ApJ, 677, 169
Vink, J. 2013, in ASP Conf. Series, vol. 470, 370 Years of Astronomy in Utrecht (San Francisco, ASP: ASP), 269
Wang, J., Navarro, J. F., Frenk, C. S., et al. 2011, MNRAS, 413, 1373
Watson, D., Christensen, L., Knudsen, K. K., et al. 2015, Natur, 519, 327
Weiß, A., de Breuck, C., Marrone, D. P., et al. 2013, ApJ, 767, 88
Windhorst, R. A., Miley, G. K., Owen, F. N., Kron, R. G., & Koo, D. C. 1985, ApJ, 289, 494
Windhorst, R. A., Mather, J., Clampin, M., et al. 2009, in Astro2010: The Astronomy and Astrophysics Decadal Survey, Science White Papers, 317
Wright, E. L., Eisenhardt, P. R. M., Mainzer, A. K., et al. 2010, AJ, 140, 1868
Wyder, T. K., Treyer, M. A., Milliard, B., et al. 2005, ApJL, 619, L15
Xia, J.-Q., Negrello, M., Lapi, A., et al. 2012, MNRAS, 422, 1324
Yun, M. S., Reddy, N. A., & Condon, J. J. 2001, ApJ, 554, 803
Zhao, D. H., Mo, H. J., Jing, Y. P., & Börner, G. 2003, MNRAS, 339, 12